

Genuinely multidimensional physical-constraints-preserving finite volume schemes for the special relativistic hydrodynamics

Dan Ling¹ and Huazhong Tang²

Abstract

This paper develops the genuinely multidimensional HLL Riemann solver for the two-dimensional special relativistic hydrodynamic equations on Cartesian meshes and studies its physical-constraint-preserving (PCP) property. Based on the resulting HLL solver, the first- and high-order accurate PCP finite volume schemes are proposed. In the high-order scheme, the WENO reconstruction, the third-order accurate strong-stability-preserving time discretizations and the PCP flux limiter are used. Several numerical results are given to demonstrate the accuracy, performance and resolution of the shock waves etc. as well as the genuinely multi-dimensional wave structures of our PCP finite volume schemes.

Keywords: Genuinely multidimensional schemes, HLL, physical-constraint-preserving property, high order accuracy, special relativistic hydrodynamics.

¹School of Mathematics and Statistics, Xi'an Jiaotong University, Xi'an, Shaanxi 710049, China. E-mail: danling@xjtu.edu.cn.

²Nanchang Hangkong University, Jiangxi Province, Nanchang 330063, P.R. China; Center for Applied Physics and Technology, HEDPS and LMAM, School of Mathematical Sciences, Peking University, Beijing 100871, P.R. China.

1 Introduction

The paper is concerned with the physical-constraints-preserving (PCP) genuinely multidimensional finite volume schemes for the special relativistic hydrodynamics (RHD), which plays a major role in astrophysics, plasma physics and nuclear physics etc., where the fluid moves at extremely high velocities near the speed of light so that the relativistic effects become important. In the (rest) laboratory frame, the two-dimensional (2D) special RHD equations governing an ideal fluid flow can be written in the divergence form

$$\frac{\partial \mathbf{U}}{\partial t} + \sum_{\ell=1}^2 \frac{\partial \mathbf{F}_\ell(\mathbf{U})}{\partial x_\ell} = 0, \quad (1.1)$$

where the conservative vector \mathbf{U} and the flux \mathbf{F}_ℓ are defined respectively by

$$\mathbf{U} = (D, \mathbf{m}, E)^T, \quad \mathbf{F}_\ell = (Du_\ell, \mathbf{m}u_\ell + p\mathbf{e}_\ell, (E+p)u_\ell)^T, \quad \ell = 1, 2, \quad (1.2)$$

here $D = \rho\gamma$, $\mathbf{m} = Dh\gamma\mathbf{u}$, $E = Dh\gamma - p$ and p are the mass, momentum and total energy relative to the laboratory frame and the gas pressure, respectively, $\mathbf{u} = (u_1, u_2)$ is the fluid velocity vector, \mathbf{e}_ℓ is the row vector denoting the ℓ -th row of the unit matrix of size 2, ρ is the rest-mass density, $\gamma = 1/\sqrt{1 - |\mathbf{u}|^2}$ is the Lorentz factor, $|\mathbf{u}|^2 = u_1^2 + u_2^2$, $h = 1 + e + \frac{p}{\rho}$ is the specific enthalpy, and e is the specific internal energy. Note that natural unit (i.e., the speed of light $c = 1$) has been used. The system (1.1) should be closed via the equation of state (EOS), which has a general form of $p = p(\rho, e)$. For simplicity, this paper considers the EOS for the perfect gas, namely

$$p = (\Gamma - 1)\rho e, \quad (1.3)$$

with the adiabatic index $\Gamma \in (1, 2]$. Such restriction on Γ is reasonable under the compressibility assumptions, and Γ is taken as 5/3 for the mildly relativistic case and 4/3 for the ultra-relativistic case. In this case, for $i = 1, 2$, the Jacobian matrix $\mathbf{A}_i(\mathbf{U}) = \partial \mathbf{F}_i / \partial \mathbf{U}$ of the system

(1.1) has 4 real eigenvalues, which are ordered from the smallest to the biggest as follows

$$\begin{aligned}\lambda_i^{(1)}(\mathbf{U}) &= \frac{u_i(1 - c_s^2) - c_s\gamma^{-1}\sqrt{1 - u_i^2 - c_s^2(|\mathbf{u}|^2 - u_i^2)}}{1 - c_s^2|\mathbf{u}|^2}, \\ \lambda_i^{(2)}(\mathbf{U}) &= \lambda_i^{(3)}(\mathbf{U}) = u_i, \\ \lambda_i^{(4)}(\mathbf{U}) &= \frac{u_i(1 - c_s^2) + c_s\gamma^{-1}\sqrt{1 - u_i^2 - c_s^2(|\mathbf{u}|^2 - u_i^2)}}{1 - c_s^2|\mathbf{u}|^2},\end{aligned}$$

where c_s is the speed of sound expressed explicitly by

$$c_s = \sqrt{\Gamma p / (\rho h)},$$

and satisfies

$$c_s^2 = \frac{\Gamma p}{\rho h} = \frac{\Gamma p}{\rho + \frac{p}{\Gamma-1} + p} = \frac{(\Gamma - 1)\Gamma p}{(\Gamma - 1)\rho + \Gamma p} < \Gamma - 1 \leq 1 = c.$$

Due to the relativistic effect, especially the appearance of the Lorentz factor, the system (1.1) becomes more strongly nonlinear than the non-relativistic case, which leads to that their analytic treatment is extremely difficult and challenging, except in some special cases, for instance, 1D Riemann problems or isentropic problems [26, 31, 24]. Because there are no explicit expressions of the primitive variable vector $\mathbf{V} = (\rho, \mathbf{u}, p)^T$ and the flux vectors \mathbf{F}_i in terms of \mathbf{U} , their values cannot be explicitly recovered from \mathbf{U} and need to solve a nonlinear equation, e.g. the following pressure equation

$$E + p = D\gamma + \frac{\Gamma}{\Gamma - 1}p\gamma^2,$$

with $\gamma = (1 - |\mathbf{m}|^2 / (E + p)^2)^{-1/2}$. Besides those, there are some physical constraints, such as $\rho > 0, p > 0$ and $E \geq D$, as well as that the velocity can not exceed the speed of light, i.e. $|\mathbf{u}| < c = 1$. For the RHD problems with large Lorentz factor or low density or low pressure, or strong discontinuity, it is easy to obtain the negative density or pressure, or the larger velocity than the speed of light in numerical computations, so that the eigenvalues of the Jacobian matrix or the Lorentz factor may become imaginary, leading directly to the ill-posedness of the discrete problem. Consequently, there is great necessity and significance to develop robust and accurate PCP numerical schemes for (1.1), whose solutions can satisfy the intrinsic physical

constraints, or belong to the admissible states set [45]

$$\mathcal{G} = \{ \mathbf{U} = (D, \mathbf{m}, E)^T \mid \rho > 0, p > 0, |\mathbf{u}| < 1 \},$$

which is equivalent to

$$\mathcal{G} = \left\{ \mathbf{U} = (D, \mathbf{m}, E)^T \mid D > 0, E - \sqrt{D^2 + |\mathbf{m}|^2} > 0 \right\}.$$

Based on that, one can prove some useful properties of \mathcal{G} , also see [45].

Lemma 1.1. *The admissible state set \mathcal{G} is convex.*

Lemma 1.2. *If assuming $\mathbf{U}, \mathbf{U}_1, \mathbf{U}_2 \in \mathcal{G}$, then:*

(i) $\kappa \mathbf{U} \in \mathcal{G}$ for all $\kappa > 0$.

(ii) $a_1 \mathbf{U}_1 + a_2 \mathbf{U}_2 \in \mathcal{G}$ for all $a_1, a_2 > 0$.

(iii) $\alpha \mathbf{U} - \mathbf{F}_i(\mathbf{U}), -\beta \mathbf{U} + \mathbf{F}_i(\mathbf{U}) \in \mathcal{G}$ for $\beta \leq \lambda_i^{(1)}(\mathbf{U}), \lambda_i^{(4)}(\mathbf{U}) \leq \alpha$, and $i = 1, 2$.

The second and third properties in Lemma 1.2 are formally different from those in Lemma 2.3 of [45]. Their proof slightly different from that of the latter can be found in Appendix A.

The study of numerical methods for the RHDs may date back to the finite difference code via artificial viscosity for the spherically symmetric general RHD equations in the Lagrangian coordinate [29, 30] and for multi-dimensional RHD equations in the Eulerian coordinate [42]. Since 1990s, the numerical study of the RHD began to attract considerable attention, see some early review articles [27, 28, 19], and various modern shock-capturing methods with an exact or approximate Riemann solver have been developed for the RHD equations. Some examples are the two-shock Riemann solver [10], the Roe Riemann solver [35], the HLL Riemann solver [20] and the HLLC Riemann solver [39] and so on. Some other higher-order accurate methods have also been well studied in the literature, e.g. the ENO (essentially non-oscillatory) and weighted ENO methods [13, 55, 38], the discontinuous Galerkin methods [34, 57, 59, 58], the adaptive moving mesh methods [21, 22, 16], and the direct Eulerian GRP schemes [52, 53, 50, 46, 54].

Recently, based on the properties of \mathcal{G} , some PCP schemes were well developed for the special RHDs. They are the high-order accurate PCP finite difference WENO schemes, discontinuous Galerkin (DG) methods and Lagrangian finite volume schemes proposed in [45, 47, 32, 43, 23]. Such works were successfully extended to the special relativistic magnetohydrodynamics (RMHD) in [48, 49], where the importance of divergence-free fields in achieving PCP methods is shown. Recently, the entropy-stable schemes were also developed for the special RHD or RMHD equations [12, 14, 15, 16, 7, 17]. Most of the above mentioned methods are built on the 1D Riemann solver, which is used to solve the local 1D Riemann problem at the cell interface by picking up flow variations that are orthogonal to the cell interface and then give the exact or approximate Riemann solution. For multi-dimensional problems, there are still confronted with enormous risks that the 1D Riemann solvers may lose their computational efficacy and efficiency to some content, because some flow features propagating transverse to the mesh boundary might be discarded, see [40] for more details. Therefore, it is necessary to capture much more flow features and then incorporate genuinely multidimensional (physical) information into numerical methods.

In the early 1990s, owing to a shift from the finite-volume approach to the fluctuation approach, the state of the art in genuinely multi-dimensional upwind differencing has made dramatic advances. A early review of multidimensional upwinding may be found in [40]. For the linearized Euler equations, a genuinely multidimensional first-order finite volume scheme was constructed in [1] by computing the exact solution of the Riemann problem for a linear hyperbolic equation obtained by linearizing the Euler equation. Up to now, there have been some further developments on multidimensional Riemann solvers and corresponding numerical schemes, including the multidimensional HLL schemes for solving the Euler equations on unstructured triangular meshes [8, 9], the genuinely multidimensional HLL-type scheme with convective pressure flux split Riemann solver [25], the multidimensional HLLC schemes for gas dynamics [41, 2], the multidimensional MuSCL solver for magnetohydrodynamics [5], the multidimensional HLLC schemes [3, 4] for hydrodynamics and magnetohydrodynamics, the

well-balanced two-dimensional HLL scheme for shallow water equations [36], and the genuinely two-dimensional scheme for compressible flows in curvilinear coordinates [33] etc. For the 2D special RHDs, the existing genuinely multidimensional scheme is the finite volume local evolution Galerkin method, developed in [44].

This paper will develop the genuinely multidimensional PCP finite volume schemes for the RHD equations (1.1). It is organized as follows. Section 2 derives the 2D HLL Riemann solver for (1.1) and studies the PCP property of its intermediate state. Section 3 presents the first-order PCP genuinely multidimensional HLL scheme and then extends it to the high-order PCP scheme by using WENO reconstruction and the third-order accurate SSP time discretizations as well as the PCP flux limiter. Section 4 conducts several numerical experiments to demonstrate the accuracy and performance of the present schemes. Section 5 concludes the paper with some remarks.

2 2D HLL Riemann solver

This section introduces the genuinely multidimensional HLL Riemann solver [2] to the 2D special RHD equations (1.1) with the EOS (1.3) on Cartesian meshes and studies its PCP property. For convenience, here and hereafter, the symbols $(\mathbf{F}_1, \mathbf{F}_2)$, (u_1, u_2) , and (x_1, x_2) will be replaced with (\mathbf{F}, \mathbf{G}) , (u, v) , and (x, y) , respectively,

Consider the 2D Riemann problem of (1.1) with the initial data as displayed in Figure 2.1, denoted by $\text{RP}(\mathbf{U}_{RU}, \mathbf{U}_{LU}, \mathbf{U}_{LD}, \mathbf{U}_{RD})$, where four constant states, \mathbf{U}_{RU} (right-up), \mathbf{U}_{LU} (left-up), \mathbf{U}_{LD} (left-down) and \mathbf{U}_{RD} (right-down) are specified in the first, second, third and fourth quadrants, respectively, and O is the coordinate origin. Denote the largest left-, right-, up- and down-moving speeds of the elementary waves emerging from the initial discontinuities by S_L, S_R, S_U, S_D , respectively. Specially, S_L and S_R are obtained as the largest left- and right-moving wave speeds in the 1D HLL solvers [39] for the two 1D Riemann problems in x -direction, denoted respectively by $\text{RP}\{\mathbf{U}_{LU}, \mathbf{U}_{RU}\}$ and $\text{RP}\{\mathbf{U}_{LD}, \mathbf{U}_{RD}\}$, and S_D and S_U are obtained by considering two 1D Riemann problems in y -direction, denoted respectively by $\text{RP}\{\mathbf{U}_{LU}, \mathbf{U}_{LD}\}$

and $\text{RP}\{\mathbf{U}_{RU}, \mathbf{U}_{RD}\}$.

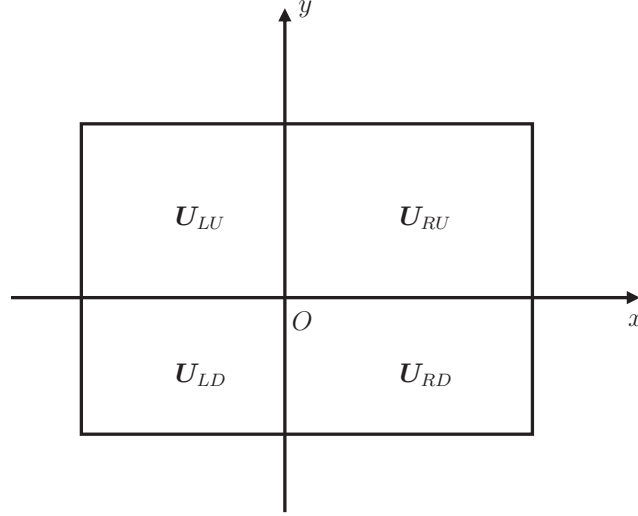


Figure 2.1: The initial data of a 2D Riemann problem at the point O .

Let us estimate the wave speeds S_L, S_R, S_D, S_U used in the 2D HLL solver. If denoting $\lambda_A^{(1)}(\mathbf{U}_{LD})$ and $\lambda_A^{(4)}(\mathbf{U}_{LD})$ as the smallest and largest eigenvalues of Jacobian matrix $\partial\mathbf{F}/\partial\mathbf{U}(\mathbf{U}_{LD})$ respectively, $\lambda_B^{(1)}(\mathbf{U}_{LD})$ and $\lambda_B^{(4)}(\mathbf{U}_{LD})$ as the smallest and largest eigenvalues of Jacobian matrix $\partial\mathbf{G}/\partial\mathbf{U}(\mathbf{U}_{LD})$ respectively, and making similar definitions at the states $\mathbf{U}_{RU}, \mathbf{U}_{LU}$, and \mathbf{U}_{RD} in the x - and y -directions, then the wave speeds S_L, S_R, S_D and S_U are respectively given by

$$\begin{aligned}
 S_L &= \alpha \min(\lambda_A^{(1)}(\mathbf{U}_{LD}), \lambda_A^{(1)}(\mathbf{U}_{RD}), \lambda_A^{(1)}(\mathbf{U}_{LU}), \lambda_A^{(1)}(\mathbf{U}_{RU})), \\
 S_R &= \alpha \max(\lambda_A^{(4)}(\mathbf{U}_{LD}), \lambda_A^{(4)}(\mathbf{U}_{RD}), \lambda_A^{(4)}(\mathbf{U}_{LU}), \lambda_A^{(4)}(\mathbf{U}_{RU})), \\
 S_D &= \alpha \min(\lambda_B^{(1)}(\mathbf{U}_{LD}), \lambda_B^{(1)}(\mathbf{U}_{RD}), \lambda_B^{(1)}(\mathbf{U}_{LU}), \lambda_B^{(1)}(\mathbf{U}_{RU})), \\
 S_U &= \alpha \max(\lambda_B^{(4)}(\mathbf{U}_{LD}), \lambda_B^{(4)}(\mathbf{U}_{RD}), \lambda_B^{(4)}(\mathbf{U}_{LU}), \lambda_B^{(4)}(\mathbf{U}_{RU})),
 \end{aligned} \tag{2.1}$$

where $\alpha \geq 1$ will be determined later. Noting that the condition $\alpha > 1$ is used to preserve the PCP property in Theorem 2.1. In practice, α is sufficiently taken as one if the PCP property is not necessary. There exist several different ways to define the wave speeds in the 1D HLL-type Riemann solvers, see e.g. [6, 18, 11]. In the following, we only discuss the case with $S_L < 0 < S_R$ and $S_D < 0 < S_U$, because in the case of that S_L and S_R (or S_D and S_U) have the same sign, our genuinely multidimensional Riemann solver will degenerate to the 1D Riemann solver.

Similar to the 1D HLL Riemann solvers, one has to derive the intermediate state \mathbf{U}^* in the approximate solution of the above 2D Riemann problem and corresponding fluxes \mathbf{F}^* and \mathbf{G}^* . For any given time $T > 0$, choose a three-dimensional cuboid $\mathbb{V}_{LRDU}(0, T)$ in the (x, y, t) space as follows: its top and bottom are rectangles with four vertices

$$(TS_L, TS_D, 0), (TS_R, TS_D, 0), (TS_L, TS_U, 0), (TS_R, TS_U, 0),$$

and

$$(TS_L, TS_D, T), (TS_R, TS_D, T), (TS_L, TS_U, T), (TS_R, TS_U, T),$$

respectively. Integrating (1.1) over $\mathbb{V}_{LRDU}(0, T)$ gives

$$\begin{aligned} \mathbf{U}^* \mathcal{A} &- \int_{TS_L}^{TS_R} \int_{TS_D}^{TS_U} \mathbf{U}(x, y, 0) dy dx \\ &+ \int_0^T \int_{TS_D}^{TS_U} \mathbf{F}(\mathbf{U}(TS_R, y, t)) dy dt - \int_0^T \int_{TS_D}^{TS_U} \mathbf{F}(\mathbf{U}(TS_L, y, t)) dy dt \\ &+ \int_0^T \int_{TS_L}^{TS_R} \mathbf{G}(\mathbf{U}(x, TS_U, t)) dx dt - \int_0^T \int_{TS_L}^{TS_R} \mathbf{G}(\mathbf{U}(x, TS_D, t)) dx dt = 0, \end{aligned} \quad (2.2)$$

where

$$\mathbf{U}^* = \frac{1}{\mathcal{A}} \int_{TS_D}^{TS_U} \int_{TS_L}^{TS_R} \mathbf{U}(x, y, T) dx dy, \quad \mathcal{A} = T^2(S_R - S_L)(S_U - S_D).$$

From (2.2), one has

$$\begin{aligned} \mathbf{U}^* &= \frac{1}{\mathcal{A}} \int_{TS_D}^{TS_U} \int_{TS_L}^{TS_R} \mathbf{U}(x, y, T) dx dy = \frac{S_R S_U \mathbf{U}_{RU} + S_L S_D \mathbf{U}_{LD} - S_R S_D \mathbf{U}_{RD} - S_L S_U \mathbf{U}_{LU}}{(S_R - S_L)(S_U - S_D)} \\ &- \frac{S_U(\mathbf{F}_{RU} - \mathbf{F}_{LU}) - S_D(\mathbf{F}_{RD} - \mathbf{F}_{LD})}{(S_R - S_L)(S_U - S_D)} - \frac{S_R(\mathbf{G}_{RU} - \mathbf{G}_{RD}) - S_L(\mathbf{G}_{LU} - \mathbf{G}_{LD})}{(S_R - S_L)(S_U - S_D)}, \end{aligned} \quad (2.3)$$

where $\mathbf{F}_{LU} = \mathbf{F}(\mathbf{U}_{LU})$ and $\mathbf{G}_{LU} = \mathbf{G}(\mathbf{U}_{LU})$, and $\mathbf{F}_{RU}, \mathbf{F}_{LD}, \mathbf{F}_{RD}, \mathbf{G}_{RU}, \mathbf{G}_{LD}, \mathbf{G}_{RD}$ are similarly defined. It is clear that the calculation of the intermediate state \mathbf{U}^* depends on four states $\mathbf{U}_{LD}, \mathbf{U}_{LU}, \mathbf{U}_{RD}$ and \mathbf{U}_{RU} , in other words, \mathbf{U}^* contains genuinely multidimensional information. In particular, if

$$\mathbf{U}_{LD} = \mathbf{U}_{LU}, \quad \mathbf{U}_{RD} = \mathbf{U}_{RU},$$

then

$$\mathbf{F}_{LD} = \mathbf{F}_{LU}, \quad \mathbf{F}_{RD} = \mathbf{F}_{RU}, \quad \mathbf{G}_{LD} = \mathbf{G}_{LU}, \quad \mathbf{G}_{RD} = \mathbf{G}_{RU},$$

and

$$\mathbf{U}^* = \frac{S_R \mathbf{U}_{RD} - S_L \mathbf{U}_{LU} + \mathbf{F}_{LD} - \mathbf{F}_{RD}}{S_R - S_L}, \quad (2.4)$$

which is indeed the intermediate state in the 1D HLL Riemann solver in [39].

Let us turn to obtain the interface fluxes \mathbf{F}^* and \mathbf{G}^* for the multidimensional Riemann solver (in the case of $S_L < 0 < S_R$ and $S_D < 0 < S_U$). Integrating respectively the system (1.1) over the left portion and the top portion (or the right and bottom portions) of the control volume $\mathbb{V}_{LRDU}(0, T)$ yields

$$\begin{aligned} \int_{TS_L}^0 \int_{TS_D}^{TS_U} \mathbf{U}(x, y, T) dy dx &= \int_{TS_L}^0 \int_{TS_D}^{TS_U} \mathbf{U}(x, y, 0) dy dx \\ &\quad - \int_0^T \int_{TS_D}^{TS_U} (\mathbf{F}(\mathbf{U}(0, y, t)) - \mathbf{F}(\mathbf{U}(TS_L, y, t))) dy dt \\ &\quad - \int_0^T \int_{TS_L}^0 (\mathbf{G}(\mathbf{U}(x, TS_U, t)) - \mathbf{G}(\mathbf{U}(x, TS_D, t))) dx dt, \end{aligned} \quad (2.5)$$

$$\begin{aligned} \int_{TS_L}^{TS_R} \int_0^{TS_U} \mathbf{U}(x, y, T) dy dx &= \int_{TS_L}^{TS_R} \int_0^{TS_U} \mathbf{U}(x, y, 0) dy dx \\ &\quad - \int_0^T \int_0^{TS_U} (\mathbf{F}(\mathbf{U}(TS_R, y, t)) - \mathbf{F}(\mathbf{U}(TS_L, y, t))) dy dt \\ &\quad - \int_0^T \int_{TS_L}^{TS_R} (\mathbf{G}(\mathbf{U}(x, TS_U, t)) - \mathbf{G}(\mathbf{U}(x, 0, t))) dx dt. \end{aligned} \quad (2.6)$$

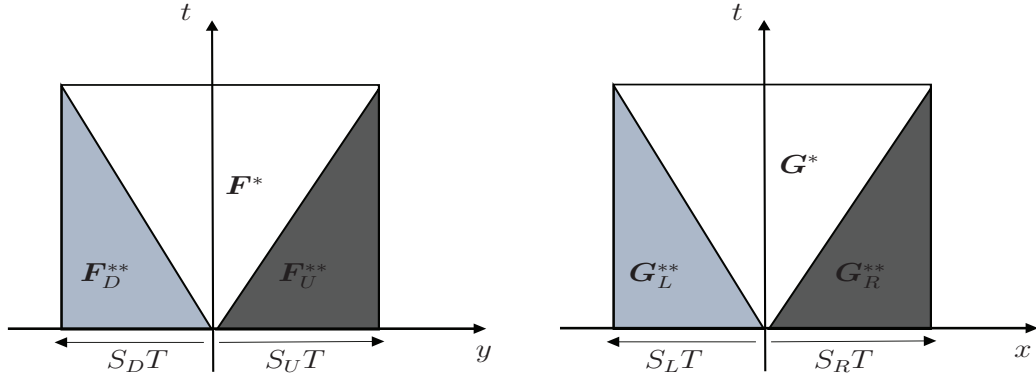


Figure 2.2: Fluxes along the faces $x = 0$ (left) and $y = 0$ (right) respectively consisting of several different portions.

As shown in the Figure 2.2, the fluxes along the faces $x = 0$ (left) and $y = 0$ (right) respectively are consisting of several different portions, so that the integrals in (2.5) and (2.6)

on the $x = 0$ and $y = 0$ faces respectively read as

$$\int_0^T \int_{TS_D}^{TS_U} \mathbf{F}(\mathbf{U}(0, y, t)) dy dt = \frac{T^2}{2} \left(S_U \mathbf{F}_U^{**} - S_D \mathbf{F}_D^{**} + (S_U - S_D) \mathbf{F}^* \right), \quad (2.7)$$

$$\int_0^T \int_{TS_L}^{TS_R} \mathbf{G}(\mathbf{U}(x, 0, t)) dx dt = \frac{T^2}{2} \left(S_R \mathbf{G}_R^{**} - S_L \mathbf{G}_L^{**} + (S_R - S_L) \mathbf{G}^* \right), \quad (2.8)$$

where \mathbf{F}_U^{**} , \mathbf{F}_D^{**} , \mathbf{G}_R^{**} , and \mathbf{G}_L^{**} are corresponding 1D HLL fluxes in the 1D HLL Riemann solver and have the specific forms of

$$\widehat{\mathbf{F}}^{\text{1d-HLL}}(\mathbf{U}_{LU}, \mathbf{U}_{RU}) := \mathbf{F}_U^{**} = \frac{1}{S_R - S_L} \left(S_R \mathbf{F}_{LU} - S_L \mathbf{F}_{RU} + S_L S_R (\mathbf{U}_{RU} - \mathbf{U}_{LU}) \right), \quad (2.9)$$

$$\widehat{\mathbf{F}}^{\text{1d-HLL}}(\mathbf{U}_{LD}, \mathbf{U}_{RD}) := \mathbf{F}_D^{**} = \frac{1}{S_R - S_L} \left(S_R \mathbf{F}_{LD} - S_L \mathbf{F}_{RD} + S_L S_R (\mathbf{U}_{RD} - \mathbf{U}_{LD}) \right), \quad (2.10)$$

$$\widehat{\mathbf{G}}^{\text{1d-HLL}}(\mathbf{U}_{RD}, \mathbf{U}_{RU}) := \mathbf{G}_R^{**} = \frac{1}{S_U - S_D} \left(S_U \mathbf{G}_{RD} - S_D \mathbf{G}_{RU} + S_D S_U (\mathbf{U}_{RU} - \mathbf{U}_{RD}) \right), \quad (2.11)$$

$$\widehat{\mathbf{G}}^{\text{1d-HLL}}(\mathbf{U}_{LD}, \mathbf{U}_{LU}) := \mathbf{G}_L^{**} = \frac{1}{S_U - S_D} \left(S_U \mathbf{G}_{LD} - S_D \mathbf{G}_{LU} + S_D S_U (\mathbf{U}_{LU} - \mathbf{U}_{LD}) \right). \quad (2.12)$$

Combining (2.3) with the relations in (2.5)-(2.12) yields

$$\mathbf{F}^* = \frac{1}{S_U - S_D} \left(S_U \mathbf{F}_U^{**} - S_D \mathbf{F}_D^{**} - \frac{2S_L S_R}{S_R - S_L} (\mathbf{G}_{RU} - \mathbf{G}_{RD} - \mathbf{G}_{LU} + \mathbf{G}_{LD}) \right), \quad (2.13)$$

$$\mathbf{G}^* = \frac{1}{S_R - S_L} \left(S_R \mathbf{G}_R^{**} - S_L \mathbf{G}_L^{**} - \frac{2S_D S_U}{S_U - S_D} (\mathbf{F}_{RU} - \mathbf{F}_{RD} - \mathbf{F}_{LU} + \mathbf{F}_{LD}) \right), \quad (2.14)$$

which are the 2D HLL fluxes in the case of $S_L < 0 < S_R$ and $S_D < 0 < S_U$. For all other cases of S_L, S_R, S_D, S_U with certain signs (either positive or negative), we can still similarly evaluate the above integrals on the $x = 0$ and $y = 0$ faces, and get the fluxes \mathbf{F}^* and \mathbf{G}^* in the multidimensional Riemann solver by (2.5) and (2.6). Hence if setting [39]

$$S_L^- = \min(S_L, 0), \quad S_R^+ = \max(S_R, 0), \quad S_D^- = \min(S_D, 0), \quad S_U^+ = \max(S_U, 0), \quad (2.15)$$

then one gets the 2D HLL fluxes \mathbf{F}^* and \mathbf{G}^* in the multidimensional Riemann solver for all situations as follows

$$\begin{aligned} \widehat{\mathbf{F}}^{\text{2d-HLL}}(\mathbf{U}_{LD}, \mathbf{U}_{LU}, \mathbf{U}_{RD}, \mathbf{U}_{RU}) &:= \mathbf{F}^* \\ &= \frac{1}{S_U^+ - S_D^-} \left(S_U^+ \mathbf{F}_U^{**} - S_D^- \mathbf{F}_D^{**} - \frac{2S_L^- S_R^+}{S_R^+ - S_L^-} (\mathbf{G}_{RU} - \mathbf{G}_{RD} - \mathbf{G}_{LU} + \mathbf{G}_{LD}) \right), \end{aligned} \quad (2.16)$$

$$\begin{aligned} \widehat{\mathbf{G}}^{2\text{d-HLL}}(\mathbf{U}_{LD}, \mathbf{U}_{LU}, \mathbf{U}_{RD}, \mathbf{U}_{RU}) &:= \mathbf{G}^* \\ &= \frac{1}{S_R^+ - S_L^-} \left(S_R^+ \mathbf{G}_R^{**} - S_L^- \mathbf{G}_L^{**} - \frac{2S_D^- S_U^+}{S_U^+ - S_D^-} (\mathbf{F}_{RU} - \mathbf{F}_{RD} - \mathbf{F}_{LU} + \mathbf{F}_{LD}) \right). \end{aligned} \quad (2.17)$$

Next, let us study the PCP property of the multidimensional HLL Riemann solver, which means that the intermediate state \mathbf{U}^* in the multidimensional Riemann solver is admissible. Only the case of $S_L < 0 < S_R, S_D < 0 < S_U$ needs to be discussed here, since all other situations (except for the non-trivial case of $S_L < 0 < S_R, S_D < 0 < S_U$) produce the 1D intermediate state which can be easily proved to be PCP according to [23]. The PCP property of the multidimensional HLL Riemann solver with (2.1) can be obtained as follows.

Theorem 2.1. *If $\mathbf{U}_{RU}, \mathbf{U}_{LU}, \mathbf{U}_{LD}, \mathbf{U}_{RD} \in \mathcal{G}$, and the wave speeds S_L, S_R, S_D, S_U are taken as (2.1) with $\alpha = 2$, then the intermediate state \mathbf{U}^* in (2.3) obtained for the multidimensional HLL Riemann solver is admissible, i.e.*

$$D^* > 0, \quad E^* > 0, \quad (E^*)^2 - (D^*)^2 - |\mathbf{m}^*|^2 > 0.$$

Proof. Assume that $S_L < 0 < S_R$ and $S_D < 0 < S_U$. Rewrite \mathbf{U}^* in (2.3) as

$$\mathbf{U}^* = \frac{1}{\mathcal{B}} \left(S_L S_D \mathbf{H}_{LD} - S_R S_D \mathbf{H}_{RD} - S_L S_U \mathbf{H}_{LU} + S_R S_U \mathbf{H}_{RU} \right),$$

with $\mathcal{B} = (S_R - S_L)(S_U - S_D)$ and

$$\begin{aligned} \mathbf{H}_{LD} &= \mathbf{U}_{LD} - \frac{1}{S_L} \mathbf{F}_{LD} - \frac{1}{S_D} \mathbf{G}_{LD}, & \mathbf{H}_{RD} &= \mathbf{U}_{RD} - \frac{1}{S_R} \mathbf{F}_{RD} - \frac{1}{S_D} \mathbf{G}_{RD}, \\ \mathbf{H}_{LU} &= \mathbf{U}_{LU} - \frac{1}{S_L} \mathbf{F}_{LU} - \frac{1}{S_U} \mathbf{G}_{LU}, & \mathbf{H}_{RU} &= \mathbf{U}_{RU} - \frac{1}{S_R} \mathbf{F}_{RU} - \frac{1}{S_U} \mathbf{G}_{RU}. \end{aligned}$$

It means that \mathbf{U}^* is a convex combination of $\mathbf{H}_{LD}, \mathbf{H}_{RD}, \mathbf{H}_{LU}, \mathbf{H}_{RU}$. Due to Lemma 1.1, it is sufficient to check whether those \mathbf{H} -terms are in the admissible set \mathcal{G} . As an example, consider the term \mathbf{H}_{LD} , which can be decomposed into two parts as follows

$$\mathbf{H}_{LD} = \mathbf{U}_{LD} - \frac{1}{S_L} \mathbf{F}_{LD} - \frac{1}{S_D} \mathbf{G}_{LD} = \frac{1}{2} \left(\mathbf{U}_{LD} - \frac{2}{S_L} \mathbf{F}_{LD} \right) + \frac{1}{2} \left(\mathbf{U}_{LD} - \frac{2}{S_D} \mathbf{G}_{LD} \right).$$

The properties (ii) and (iii) in Lemma 1.2 show the admissibility of $\mathbf{U}_{LD} - \frac{2}{S_L} \mathbf{F}_{LD}$ and $\mathbf{U}_{LD} - \frac{2}{S_D} \mathbf{G}_{LD}$ so is \mathbf{H}_{LD} . Similarly, one can show that other \mathbf{H} -terms are also admissible. The proof is completed. \square

3 Numerical schemes

This section presents the first- and high-order accurate PCP finite volume schemes with the above multidimensional HLL Riemann solver for the special RHD equations (1.1).

3.1 First-order PCP scheme

Consider 2D Cartesian mesh in (x, y) space $\{(x_{i+\frac{1}{2}}, y_{j+\frac{1}{2}}) | \Delta x_i = x_{i+\frac{1}{2}} - x_{i-\frac{1}{2}}, \Delta y_j = y_{j+\frac{1}{2}} - y_{j-\frac{1}{2}}, i, j \in \mathbb{Z}\}$ and define the rectangular cell $I_{ij} = [x_{i-\frac{1}{2}}, x_{i+\frac{1}{2}}] \times [y_{j-\frac{1}{2}}, y_{j+\frac{1}{2}}]$. Assume that $t_{n+1} = t_n + \Delta t^n$ with $t_0 = 0$, where Δt^n is the time step-size at $t = t_n$ and to be determined later, $n = 0, 1, 2, \dots$. The numerical solutions at t_n are reconstructed as a piecewise constant function by using the (approximate) cell average values \bar{U}_{ij}^n of \mathbf{U} at t_n over the cell I_{ij} .

Integrating the RHD system (1.1) over the cell $I_{ij} \times [t_n, t_{n+1})$ obtains the following finite volume scheme

$$\bar{U}_{ij}^{n+1} = \bar{U}_{ij}^n - \frac{\Delta t^n}{\Delta x_i} (\hat{\mathbf{F}}_{i+\frac{1}{2},j} - \hat{\mathbf{F}}_{i-\frac{1}{2},j}) - \frac{\Delta t^n}{\Delta y_j} (\hat{\mathbf{G}}_{i,j+\frac{1}{2}} - \hat{\mathbf{G}}_{i,j-\frac{1}{2}}), \quad (3.1)$$

where $\hat{\mathbf{F}}_{i+\frac{1}{2},j}$ and $\hat{\mathbf{G}}_{i,j+\frac{1}{2}}$ are the numerical fluxes approximating the flux integrals

$$\begin{aligned} I_{i+\frac{1}{2},j}^y &:= \frac{1}{\Delta t^n \Delta y_j} \int_{t_n}^{t_{n+1}} \int_{y_{j-\frac{1}{2}}}^{y_{j+\frac{1}{2}}} \mathbf{F}(\mathbf{U}(x_{i+\frac{1}{2}}, y, t_n)) dy dt, \\ I_{i,j+\frac{1}{2}}^x &:= \frac{1}{\Delta t^n \Delta x_i} \int_{t_n}^{t_{n+1}} \int_{x_{i-\frac{1}{2}}}^{x_{i+\frac{1}{2}}} \mathbf{G}(\mathbf{U}(x, y_{j+\frac{1}{2}}, t_n)) dx dt, \end{aligned} \quad (3.2)$$

respectively, and Δt^n is determined by the CFL type condition

$$\Delta t^n \leq \sigma \min_{i,j} \left\{ \frac{\Delta x_i}{\max(|\lambda_A^{(1)}(\bar{U}_{ij}^n)|, |\lambda_A^{(4)}(\bar{U}_{ij}^n)|)}, \frac{\Delta y_j}{\max(|\lambda_B^{(1)}(\bar{U}_{ij}^n)|, |\lambda_B^{(4)}(\bar{U}_{ij}^n)|)} \right\}, \quad (3.3)$$

here the CFL number $\sigma \leq \frac{1}{2}$. Noting that (3.1) can also be derived by integrating the RHD system (1.1) over the cell $I_{ij} \times [t_n, t_{n+1})$. Following [2], see Figure 2.2, the numerical fluxes $\hat{\mathbf{F}}$ and $\hat{\mathbf{G}}$ are contributed by the 1D Riemann solver at the center of the cell edge and the 2D Riemann solver at two endpoints of the cell edge. For example, the numerical flux $\hat{\mathbf{F}}_{i+\frac{1}{2},j}$ consists of three parts: $\mathbf{F}_{i+\frac{1}{2},j}^{**}$ computed from the 1D HLL Riemann solver at the point $(x_{i+\frac{1}{2}}, y_j)$ and

$\mathbf{F}_{i+\frac{1}{2},j-\frac{1}{2}}^*$, $\mathbf{F}_{i+\frac{1}{2},j+\frac{1}{2}}^*$ computed from the 2D HLL Riemann solvers at $(x_{i+\frac{1}{2}}, y_{j-\frac{1}{2}})$ and $(x_{i+\frac{1}{2}}, y_{j+\frac{1}{2}})$, respectively, where

$$\begin{aligned}\mathbf{F}_{i+\frac{1}{2},j}^{**} &= \widehat{\mathbf{F}}^{\text{1d-HLL}}(\mathbf{U}_{i+\frac{1}{2},j}^L, \mathbf{U}_{i+\frac{1}{2},j}^R), \\ \mathbf{F}_{i+\frac{1}{2},j\pm\frac{1}{2}}^* &= \widehat{\mathbf{F}}^{\text{2d-HLL}}(\mathbf{U}_{i+\frac{1}{2},j\pm\frac{1}{2}}^{LD}, \mathbf{U}_{i+\frac{1}{2},j\pm\frac{1}{2}}^{LU}, \mathbf{U}_{i+\frac{1}{2},j\pm\frac{1}{2}}^{RD}, \mathbf{U}_{i+\frac{1}{2},j\pm\frac{1}{2}}^{RU}),\end{aligned}\quad (3.4)$$

with $\mathbf{U}_{i+\frac{1}{2},j}^L, \mathbf{U}_{i+\frac{1}{2},j}^R$ being the left and right limited approximations of \mathbf{U} at the center of the edge $x = x_{i+\frac{1}{2}}$, and $\mathbf{U}_{i+\frac{1}{2},j\pm\frac{1}{2}}^{LD}, \mathbf{U}_{i+\frac{1}{2},j\pm\frac{1}{2}}^{RD}, \mathbf{U}_{i+\frac{1}{2},j\pm\frac{1}{2}}^{LU}, \mathbf{U}_{i+\frac{1}{2},j\pm\frac{1}{2}}^{RU}$ being the left-down, right-down, left-up and right-up limited approximations of \mathbf{U} at the node $(x_{i+\frac{1}{2}}, y_{j\pm\frac{1}{2}})$, defined respectively by

$$\begin{aligned}\mathbf{U}_{i+\frac{1}{2},j}^L &= \overline{\mathbf{U}}_{ij}, & \mathbf{U}_{i+\frac{1}{2},j}^R &= \overline{\mathbf{U}}_{i+1,j}, & \mathbf{U}_{i+\frac{1}{2},j+\frac{1}{2}}^{LD} &= \overline{\mathbf{U}}_{ij}, \\ \mathbf{U}_{i+\frac{1}{2},j+\frac{1}{2}}^{RD} &= \overline{\mathbf{U}}_{i+1,j}, & \mathbf{U}_{i+\frac{1}{2},j+\frac{1}{2}}^{LU} &= \overline{\mathbf{U}}_{i,j+1}, & \mathbf{U}_{i+\frac{1}{2},j+\frac{1}{2}}^{RU} &= \overline{\mathbf{U}}_{i+1,j+1}.\end{aligned}\quad (3.5)$$

In practice, for the case of $S_D < 0 < S_U$, see the left schematics of -eps-converted-to.pdf 2.2 and 3.1, the numerical flux $\widehat{\mathbf{F}}_{i+\frac{1}{2},j}$ may be derived by

$$\begin{aligned}I_{i+\frac{1}{2},j}^y &= \frac{1}{\Delta t^n \Delta y_j} \int_{t_n}^{t_{n+1}} \left\{ \int_{y_{j-\frac{1}{2}}}^{y_{j-\frac{1}{2}}^U} + \int_{y_{j-\frac{1}{2}}^D}^{y_{j+\frac{1}{2}}^D} + \int_{y_{j+\frac{1}{2}}^D}^{y_{j+\frac{1}{2}}} \right\} \mathbf{F}(\mathbf{U}(x_{i+\frac{1}{2}}, y, t_n)) dy dt \\ &\approx \frac{S_{U,i+\frac{1}{2},j-\frac{1}{2}} \Delta t^n}{2\Delta y_j} \mathbf{F}_{i+\frac{1}{2},j-\frac{1}{2}}^* + \left(1 - \frac{(S_{U,i+\frac{1}{2},j-\frac{1}{2}} - S_{D,i+\frac{1}{2},j+\frac{1}{2}}) \Delta t^n}{2\Delta y_j} \right) \mathbf{F}_{i+\frac{1}{2},j}^{**} - \frac{S_{D,i+\frac{1}{2},j+\frac{1}{2}} \Delta t^n}{2\Delta y_j} \mathbf{F}_{i+\frac{1}{2},j+\frac{1}{2}}^*,\end{aligned}$$

under the assumption of $\frac{(S_{U,i+\frac{1}{2},j-\frac{1}{2}} - S_{D,i+\frac{1}{2},j+\frac{1}{2}}) \Delta t^n}{2\Delta y_j} \leq 1$, where $y_{j-\frac{1}{2}}^U := y_{j-\frac{1}{2}} + S_{U,i+\frac{1}{2},j-\frac{1}{2}} \Delta t^n$, $y_{j+\frac{1}{2}}^D := y_{j+\frac{1}{2}} + S_{D,i+\frac{1}{2},j+\frac{1}{2}} \Delta t^n$. Similarly, the numerical flux $\widehat{\mathbf{G}}_{i,j+\frac{1}{2}}$ consists of $\mathbf{G}_{i,j+\frac{1}{2}}^{**}$ and $\mathbf{G}_{i\pm\frac{1}{2},j+\frac{1}{2}}^*$, which are computed from the 1D HLL Riemann solver at $(x_i, y_{j+\frac{1}{2}})$ and the 2D HLL Riemann solvers at $(x_{i-\frac{1}{2}}, y_{j+\frac{1}{2}})$ and $(x_{i+\frac{1}{2}}, y_{j+\frac{1}{2}})$ respectively, and may also be derived by approximating the second flux integral in (3.2) under the assumption of

$\frac{(S_{R,i-\frac{1}{2},j+\frac{1}{2}} - S_{L,i+\frac{1}{2},j+\frac{1}{2}}) \Delta t^n}{2\Delta x_i} \leq 1$. With the help of the definitions of $S_L^-, S_R^+, S_D^-, S_U^+$ in (2.15), the numerical fluxes $\widehat{\mathbf{F}}$ and $\widehat{\mathbf{G}}$ in (3.1) are finally given by

$$\begin{aligned}\widehat{\mathbf{F}}_{i+\frac{1}{2},j} &= \frac{\Delta t^n}{2\Delta y_j} S_{U,i+\frac{1}{2},j-\frac{1}{2}}^+ \mathbf{F}_{i+\frac{1}{2},j-\frac{1}{2}}^* - \frac{\Delta t^n}{2\Delta y_j} S_{D,i+\frac{1}{2},j+\frac{1}{2}}^- \mathbf{F}_{i+\frac{1}{2},j+\frac{1}{2}}^* \\ &\quad + \left(1 - \frac{\Delta t^n}{2\Delta y_j} (S_{U,i+\frac{1}{2},j-\frac{1}{2}}^+ - S_{D,i+\frac{1}{2},j+\frac{1}{2}}^-) \right) \mathbf{F}_{i+\frac{1}{2},j}^{**}, \\ \widehat{\mathbf{G}}_{i,j+\frac{1}{2}} &= \frac{\Delta t^n}{2\Delta x_i} S_{R,i-\frac{1}{2},j+\frac{1}{2}}^+ \mathbf{G}_{i-\frac{1}{2},j+\frac{1}{2}}^* - \frac{\Delta t^n}{2\Delta x_i} S_{L,i+\frac{1}{2},j+\frac{1}{2}}^- \mathbf{G}_{i+\frac{1}{2},j+\frac{1}{2}}^*\end{aligned}\quad (3.6)$$

$$+ \left(1 - \frac{\Delta t^n}{2\Delta x_i} (S_{R,i-\frac{1}{2},j+\frac{1}{2}}^+ - S_{L,i+\frac{1}{2},j+\frac{1}{2}}^-) \right) \mathbf{G}_{i,j+\frac{1}{2}}^{**}, \quad (3.7)$$

under the time stepsize constraint

$$\Delta t^n \leq \min_{i,j} \left(\frac{2\Delta x_i}{S_{R,i-\frac{1}{2},j\pm\frac{1}{2}}^+ - S_{L,i+\frac{1}{2},j\pm\frac{1}{2}}^-}, \frac{2\Delta y_j}{S_{U,i\pm\frac{1}{2},j-\frac{1}{2}}^+ - S_{D,i\pm\frac{1}{2},j+\frac{1}{2}}^-} \right), \quad (3.8)$$

which is weaker than (3.3).

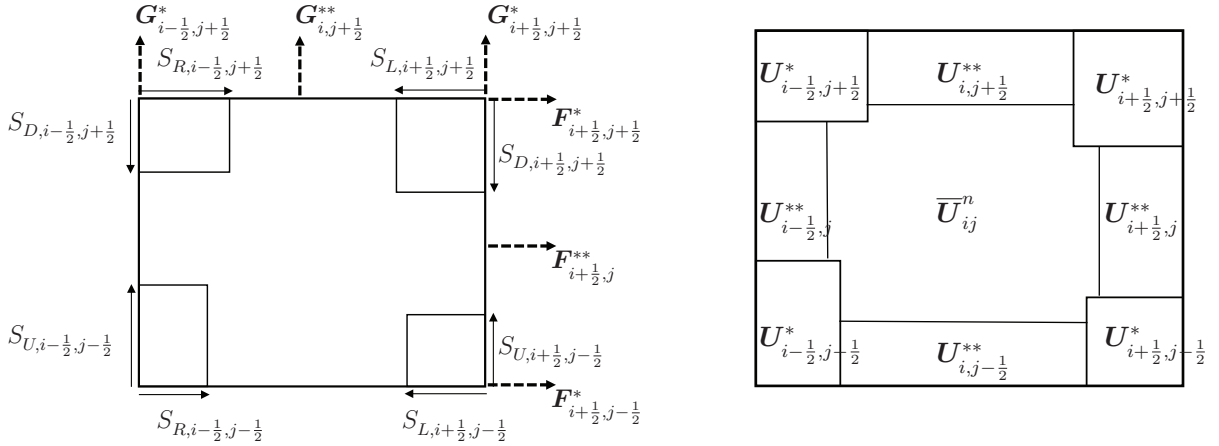


Figure 3.1: Illustration for the numerical fluxes (left) and approximate solution (right) for the numerical scheme (3.1).

Let us now discuss the PCP property of the scheme (3.1) with the numerical fluxes (3.6) and (3.7). According to the 1D and 2D HLL Riemann solvers, under the CFL condition (3.3) with $\sigma \leq \frac{1}{2}$, $\bar{\mathbf{U}}_{ij}^{n+1}$ in the scheme (3.1) can be written as an exact integration of those approximate Riemann solutions over the cell I_{ij} , namely

$$\begin{aligned} \bar{\mathbf{U}}_{ij}^{n+1} = & \frac{1}{\Delta x_i \Delta y_j} \left(\int_{\Omega_1} R_h(x/t, y/t, \bar{\mathbf{U}}_{i-1,j-1}^n, \bar{\mathbf{U}}_{i-1,j}^n, \bar{\mathbf{U}}_{i,j-1}^n, \bar{\mathbf{U}}_{ij}^n) dx dy + \int_{\Omega_5} \tilde{R}_h(x/t, \bar{\mathbf{U}}_{i-1,j}^n, \bar{\mathbf{U}}_{ij}^n) dx dy \right. \\ & + \int_{\Omega_2} R_h(x/t, y/t, \bar{\mathbf{U}}_{i,j-1}^n, \bar{\mathbf{U}}_{i,j}^n, \bar{\mathbf{U}}_{i+1,j-1}^n, \bar{\mathbf{U}}_{i+1,j}^n) dx dy + \int_{\Omega_6} \tilde{R}_h(x/t, \bar{\mathbf{U}}_{ij}^n, \bar{\mathbf{U}}_{i+1,j}^n) dx dy \\ & + \int_{\Omega_3} R_h(x/t, y/t, \bar{\mathbf{U}}_{i-1,j}^n, \bar{\mathbf{U}}_{i-1,j+1}^n, \bar{\mathbf{U}}_{ij}^n, \bar{\mathbf{U}}_{i,j+1}^n) dx dy + \int_{\Omega_7} \tilde{R}_h(y/t, \bar{\mathbf{U}}_{i,j-1}^n, \bar{\mathbf{U}}_{ij}^n) dx dy \\ & + \int_{\Omega_4} R_h(x/t, y/t, \bar{\mathbf{U}}_{ij}^n, \bar{\mathbf{U}}_{i,j+1}^n, \bar{\mathbf{U}}_{i+1,j}^n, \bar{\mathbf{U}}_{i+1,j+1}^n) dx dy + \int_{\Omega_8} \tilde{R}_h(y/t, \bar{\mathbf{U}}_{ij}^n, \bar{\mathbf{U}}_{i,j+1}^n) dx dy \\ & \left. + \int_{I_{ij} \setminus \bigcup_{m=1}^8 \Omega_m} \bar{\mathbf{U}}_{ij}^n dx dy \right), \end{aligned}$$

where $R_h(x/t, y/t, \bar{U}_1, \bar{U}_2, \bar{U}_3, \bar{U}_4)$ is the approximate solution of the 2D Riemann problem with four initial states $\bar{U}_1, \bar{U}_2, \bar{U}_3$ and \bar{U}_4 , $\tilde{R}_h(z/t, \bar{U}_1, \bar{U}_2)$ is the approximate solution of 1D Riemann problems in z -direction with two initial states \bar{U}_1, \bar{U}_2 , $z = x, y$, and

$$\begin{aligned}
\Omega_1 &= [x_{i-\frac{1}{2}}, x_{i-\frac{1}{2}} + \Delta t^n S_{R,i-\frac{1}{2},j-\frac{1}{2}}^+] \times [y_{j-\frac{1}{2}}, y_{j-\frac{1}{2}} + \Delta t^n S_{U,i-\frac{1}{2},j-\frac{1}{2}}^+], \\
\Omega_2 &= [x_{i+\frac{1}{2}} + \Delta t^n S_{L,i+\frac{1}{2},j-\frac{1}{2}}^-, x_{i+\frac{1}{2}}] \times [y_{j-\frac{1}{2}}, y_{j-\frac{1}{2}} + \Delta t^n S_{U,i+\frac{1}{2},j-\frac{1}{2}}^+], \\
\Omega_3 &= [x_{i-\frac{1}{2}}, x_{i-\frac{1}{2}} + \Delta t^n S_{R,i-\frac{1}{2},j-\frac{1}{2}}^+] \times [y_{j+\frac{1}{2}} + \Delta t^n S_{D,i-\frac{1}{2},j+\frac{1}{2}}^-, y_{j+\frac{1}{2}}], \\
\Omega_4 &= [x_{i+\frac{1}{2}} + \Delta t^n S_{L,i+\frac{1}{2},j-\frac{1}{2}}^-, x_{i+\frac{1}{2}}] \times [y_{j+\frac{1}{2}} + \Delta t^n S_{D,i+\frac{1}{2},j+\frac{1}{2}}^-, y_{j+\frac{1}{2}}], \\
\Omega_5 &= [x_{i-\frac{1}{2}}, x_{i-\frac{1}{2}} + \Delta t^n S_1^+] \times [y_{j-\frac{1}{2}} + \Delta t^n S_{U,i-\frac{1}{2},j+\frac{1}{2}}^+, y_{j+\frac{1}{2}} + \Delta t^n S_{D,i-\frac{1}{2},j+\frac{1}{2}}^-], \\
\Omega_6 &= [x_{i+\frac{1}{2}} + \Delta t^n S_2^-, x_{i+\frac{1}{2}}] \times [y_{j-\frac{1}{2}} + \Delta t^n S_{U,i+\frac{1}{2},j+\frac{1}{2}}^+, y_{j+\frac{1}{2}} + \Delta t^n S_{D,i+\frac{1}{2},j+\frac{1}{2}}^-], \\
\Omega_7 &= [x_{i-\frac{1}{2}} + \Delta t^n S_{R,i-\frac{1}{2},j-\frac{1}{2}}^+, x_{i+\frac{1}{2}} + \Delta t^n S_{L,i+\frac{1}{2},j-\frac{1}{2}}^+] \times [y_{j-\frac{1}{2}}, y_{j-\frac{1}{2}} + \Delta t^n S_3^+], \\
\Omega_8 &= [x_{i-\frac{1}{2}} + \Delta t^n S_{R,i-\frac{1}{2},j+\frac{1}{2}}^+, x_{i+\frac{1}{2}} + \Delta t^n S_{L,i+\frac{1}{2},j+\frac{1}{2}}^+] \times [y_{j+\frac{1}{2}}, y_{j+\frac{1}{2}} + \Delta t^n S_4^-, y_{j+\frac{1}{2}}],
\end{aligned}$$

here $S^- = \min(0, S)$, $S^+ = \max(0, S)$, S_1 and S_2 are the largest and smallest wave speeds in the 1D Riemann HLL solver for two x -directional Riemann problems denoted by $\text{RP}\{\bar{U}_{i-1,j}^n, \bar{U}_{ij}^n\}$ and $\text{RP}\{\bar{U}_{ij}^n, \bar{U}_{i+1,j}^n\}$, S_3 and S_4 are the largest and smallest wave speeds in the 1D Riemann HLL solver for two y -directional Riemann problems denoted by $\text{RP}\{\bar{U}_{i,j-1}^n, \bar{U}_{ij}^n\}$ and $\text{RP}\{\bar{U}_{ij}^n, \bar{U}_{i,j+1}^n\}$. Based on the aforementioned 1D and 2D HLL Riemann solvers, one can get

$$\begin{aligned}
\int_{\Omega_1} R_h(x/t, y/t, \bar{U}_{i-1,j-1}^n, \bar{U}_{i-1,j}^n, \bar{U}_{i,j-1}^n, \bar{U}_{ij}^n) dx dy &= |\Omega_1| \mathbf{U}_{i-\frac{1}{2},j-\frac{1}{2}}^*, \\
\int_{\Omega_2} R_h(x/t, y/t, \bar{U}_{i,j-1}^n, \bar{U}_{i,j}^n, \bar{U}_{i+1,j-1}^n, \bar{U}_{i+1,j}^n) dx dy &= |\Omega_2| \mathbf{U}_{i+\frac{1}{2},j-\frac{1}{2}}^*, \\
\int_{\Omega_3} R_h(x/t, y/t, \bar{U}_{i-1,j}^n, \bar{U}_{i-1,j+1}^n, \bar{U}_{ij}^n, \bar{U}_{i,j+1}^n) dx dy &= |\Omega_3| \mathbf{U}_{i-\frac{1}{2},j+\frac{1}{2}}^*, \\
\int_{\Omega_4} R_h(x/t, y/t, \bar{U}_{ij}^n, \bar{U}_{i,j+1}^n, \bar{U}_{i+1,j}^n, \bar{U}_{i+1,j+1}^n) dx dy &= |\Omega_4| \mathbf{U}_{i+\frac{1}{2},j+\frac{1}{2}}^*, \\
\int_{\Omega_5} \tilde{R}_h(x/t, \bar{U}_{i-1,j}^n, \bar{U}_{ij}^n) dx dy &= |\Omega_5| \mathbf{U}_{i-\frac{1}{2},j}^{**}, \quad \int_{\Omega_6} \tilde{R}_h(x/t, \bar{U}_{ij}^n, \bar{U}_{i+1,j}^n) dx dy = |\Omega_6| \mathbf{U}_{i+\frac{1}{2},j}^{**}, \\
\int_{\Omega_7} \tilde{R}_h(y/t, \bar{U}_{i,j-1}^n, \bar{U}_{ij}^n) dx dy &= |\Omega_7| \mathbf{U}_{i,j-\frac{1}{2}}^{**}, \quad \int_{\Omega_8} \tilde{R}_h(y/t, \bar{U}_{ij}^n, \bar{U}_{i,j+1}^n) dx dy = |\Omega_8| \mathbf{U}_{i,j+\frac{1}{2}}^{**},
\end{aligned}$$

where $|\Omega_m|$ stands for the area of the domain Ω_m , $m = 1, 2, \dots, 8$, the terms with the superscripts “*” and “**” are obtained in the 2D and 1D HLL Riemann solvers, respectively. Clearly,

for the the non-trivial case of $S_L < 0 < S_R, S_D < 0 < S_U$, the updated solution \overline{U}_{ij}^{n+1} can be reformulated as a convex combination of nine terms: $\overline{U}_{ij}^n, \mathbf{U}_{i-\frac{1}{2},j-\frac{1}{2}}^*, \mathbf{U}_{i+\frac{1}{2},j-\frac{1}{2}}^*, \mathbf{U}_{i-\frac{1}{2},j+\frac{1}{2}}^*, \mathbf{U}_{i+\frac{1}{2},j+\frac{1}{2}}^*$ and $\mathbf{U}_{i-\frac{1}{2},j}^{**}, \mathbf{U}_{i+\frac{1}{2},j}^{**}, \mathbf{U}_{i,j-\frac{1}{2}}^{**}, \mathbf{U}_{i,j+\frac{1}{2}}^{**}$, see the right schematic of Figure 3.1. On the other hand, it is obvious to know that each term in the convex combination is admissible, see Section 2, so that the numerical solution \overline{U}_{ij}^{n+1} to the first-order scheme (3.1) with (3.5)-(3.7) is also admissible. We conclude such result in the following theorem.

Theorem 3.1. *If $\overline{U}_{ij}^n \in \mathcal{G}$, for all $i, j \in \mathbb{Z}$, and the wave speeds S_D, S_U, S_L, S_R are estimated by (2.1) with $\alpha = 2$, then \overline{U}_{ij}^{n+1} obtained by the first-order scheme (3.1) with (3.5)-(3.7) and the multidimensional Riemann solver belongs to the admissible state set \mathcal{G} under the time step size restriction (3.3) with $\sigma \leq \frac{1}{2}$.*

Remark 3.1. *The numerical fluxes in (3.6)-(3.7) may be further extended as*

$$\widehat{F}_{i+\frac{1}{2},j} = \alpha \mathbf{F}_{i+\frac{1}{2},j-\frac{1}{2}}^* + \beta \mathbf{F}_{i+\frac{1}{2},j+\frac{1}{2}}^* + (1 - (\alpha + \beta)) \mathbf{F}_{i+\frac{1}{2},j}^{**}, \quad (3.9)$$

$$\widehat{G}_{i,j+\frac{1}{2}} = \tilde{\alpha} \mathbf{G}_{i-\frac{1}{2},j+\frac{1}{2}}^* + \tilde{\beta} \mathbf{G}_{i+\frac{1}{2},j+\frac{1}{2}}^* + \left(1 - (\tilde{\alpha} + \tilde{\beta})\right) \mathbf{G}_{i,j+\frac{1}{2}}^{**}, \quad (3.10)$$

which are similarly obtained by approximating the flux integrals $I_{i+\frac{1}{2},j}^y$ and $I_{i,j+\frac{1}{2}}^x$, for example, in the case of $S_D < 0 < S_U, S_L < 0 < S_R$,

$$\begin{aligned} I_{i+\frac{1}{2},j}^y &\approx \alpha \mathbf{F}_{i+\frac{1}{2},j-\frac{1}{2}}^* + (1 - (\alpha + \beta)) \mathbf{F}_{i+\frac{1}{2},j}^{**} + \beta \mathbf{F}_{i+\frac{1}{2},j+\frac{1}{2}}^*, \\ I_{i,j+\frac{1}{2}}^x &\approx \tilde{\alpha} \mathbf{G}_{i-\frac{1}{2},j+\frac{1}{2}}^* + (1 - (\tilde{\alpha} + \tilde{\beta})) \mathbf{G}_{i,j+\frac{1}{2}}^{**} + \tilde{\beta} \mathbf{G}_{i+\frac{1}{2},j+\frac{1}{2}}^*, \end{aligned}$$

where $\alpha, \beta, \tilde{\alpha}$, and $\tilde{\beta}$ satisfy $\alpha, \beta \geq 0, \alpha + \beta \leq 1, \tilde{\alpha}, \tilde{\beta} \geq 0$, and $\tilde{\alpha} + \tilde{\beta} \leq 1$. Obviously, those may be related to the weights of the Simpson rule or the three-point Gauss-Lobatto quadrature. It is worth noting that the PCP property as in Theorem 3.1 may be preserved by the scheme (3.1) with (3.9)-(3.10) under some suitable CFL-type conditions.

3.2 High-order PCP scheme

This subsection develops the high-order accurate PCP scheme for (1.1) with the previous 2D HLL Riemann solver, the high-order initial reconstruction, the high-order approximation of

the flux integrals (3.2), and the PCP flux limiter as well as the explicit SSP Runge-Kutta time discretization. Here the Gauss-Lobatto quadrature with K points and weights $\{\omega_\alpha : \sum_{\alpha=1}^K \omega_\alpha = 1\}$ is used to calculate the flux integrals (3.2) in order to involve the 2D HLL Riemann solver, where $2K - 3 \geq r$ for a $(r + 1)$ th-order accurate scheme for (1.1).

Denote the Gauss-Lobatto quadrature points on the intervals $[x_{i-\frac{1}{2}}, x_{i+\frac{1}{2}}]$ and $[y_{j-\frac{1}{2}}, y_{j+\frac{1}{2}}]$ respectively as follows

$$S_i^x = \{x_i^\alpha, \alpha = 1, 2, \dots, K\}, \quad (3.11)$$

and

$$S_j^y = \{y_j^\beta, \beta = 1, 2, \dots, K\}, \quad (3.12)$$

and define the Gauss-Lobatto quadrature points on the cell I_{ij} by

$$S_{ij} = \{(x_i^\alpha, y_j^\beta), \alpha, \beta = 1, 2, \dots, K\}.$$

By using the (approximate) cell average values $\bar{\mathbf{U}}_{ij}^n$ of \mathbf{U} at t_n over the cell I_{ij} , the dimension by dimension WENO reconstruction [37] with the local characteristic decomposition is performed in the x - and y -directions respectively to get the high-order WENO approximations of \mathbf{U} at those quadrature points S_i^x, S_j^y, S_{ij} , denoted respectively by

$$\mathbf{U}_{ij}^n(x_{i+\frac{1}{2}}, y_j^\beta), \quad \mathbf{U}_{ij}^n(x_i^\alpha, y_{j+\frac{1}{2}}), \quad \mathbf{U}_{ij}^n(x_i^\alpha, y_j^\beta).$$

The readers are also referred to [57] for details. The numerical solutions at t_n can further be reconstructed as a piecewise polynomial with $\mathbf{U}_{ij}^n(x, y)$ for $(x, y) \in I_{ij}$ by using the Lagrangian interpolation with the point values $\mathbf{U}_{ij}^n(x_i^\alpha, y_j^\beta)$.

Based on the above reconstruction and the Gauss-Lobatto quadrature with K points, the flux integrals in (3.2) can be approximately calculated as follows

$$\begin{aligned} I_{i+\frac{1}{2}, j}^y &\approx \sum_{\beta=1}^K \omega_\beta \mathbf{F}(\mathbf{U}_{ij}^n(x_{i+\frac{1}{2}}, y_j^\beta)) \approx \sum_{\beta=1}^K \omega_\beta \widehat{\mathbf{F}}_{i+\frac{1}{2}, j^\beta} =: \widehat{\mathbf{F}}_{i+\frac{1}{2}, j}^{\text{high}}, \\ I_{i, j+\frac{1}{2}}^x &\approx \sum_{\alpha=1}^K \tilde{\omega}_\alpha \mathbf{G}(\mathbf{U}_{ij}^n(x_i^\alpha, y_{j+\frac{1}{2}})) \approx \sum_{\alpha=1}^K \tilde{\omega}_\alpha \widehat{\mathbf{G}}_{i^\alpha, j+\frac{1}{2}} =: \widehat{\mathbf{G}}_{i, j+\frac{1}{2}}^{\text{high}}, \end{aligned} \quad (3.13)$$

where $\{\omega_\beta\}$ and $\{\tilde{\omega}_\alpha\}$ denote the quadrature weights for $I_{i+\frac{1}{2},j}^y$ and $I_{i,j+\frac{1}{2}}^x$, $\widehat{\mathbf{F}}_{i+\frac{1}{2},j_\beta}$ and $\widehat{\mathbf{G}}_{i_\alpha,j+\frac{1}{2}}$ denote the numerical fluxes, evaluated at quadrature points $(x_{i+\frac{1}{2}}, y_j^\beta)$ and $(x_i^\alpha, y_{j+\frac{1}{2}})$ with the 1D or 2D HLL Riemann solver, respectively. Specially, we have

$$\begin{aligned}\widehat{\mathbf{F}}_{i\pm\frac{1}{2},j}^{\text{high}} &= \sum_{\beta=1}^K \omega_\beta \widehat{\mathbf{F}}_{i\pm\frac{1}{2},j_\beta} = \omega_1 (\mathbf{F}_{i\pm\frac{1}{2},j-\frac{1}{2}}^* + \mathbf{F}_{i\pm\frac{1}{2},j+\frac{1}{2}}^*) + \sum_{\beta=2}^{K-1} \omega_\beta \mathbf{F}_{i\pm\frac{1}{2},j_\beta}^{**}, \\ \widehat{\mathbf{G}}_{i,j\pm\frac{1}{2}}^{\text{high}} &= \sum_{\alpha=1}^K \tilde{\omega}_\alpha \widehat{\mathbf{G}}_{i_\alpha,j\pm\frac{1}{2}} = \tilde{\omega}_1 (\mathbf{G}_{i-\frac{1}{2},j\pm\frac{1}{2}}^* + \mathbf{G}_{i+\frac{1}{2},j\pm\frac{1}{2}}^*) + \sum_{\alpha=2}^{K-1} \tilde{\omega}_\alpha \mathbf{G}_{i_\alpha,j\pm\frac{1}{2}}^{**},\end{aligned}\quad (3.14)$$

Then the scheme (3.1) becomes

$$\overline{\mathbf{U}}_{ij}^{n+1} = \overline{\mathbf{U}}_{ij}^n - \frac{\Delta t^n}{\Delta x_i} (\widehat{\mathbf{F}}_{i+\frac{1}{2},j}^{\text{high}} - \widehat{\mathbf{F}}_{i-\frac{1}{2},j}^{\text{high}}) - \frac{\Delta t^n}{\Delta y_j} (\widehat{\mathbf{G}}_{i,j+\frac{1}{2}}^{\text{high}} - \widehat{\mathbf{G}}_{i,j-\frac{1}{2}}^{\text{high}}). \quad (3.15)$$

In general, the high-order accurate scheme (3.15) with the numerical fluxes (3.14) does not satisfy the PCP property, namely, we can not guarantee that $(\overline{\mathbf{U}}_{ij}^{n+1})^{\text{high}} := \overline{\mathbf{U}}_{ij}^{n+1}$ obtained from (3.15) belongs to the admissible set \mathcal{G} . Here, we utilize the PCP flux limiter in [45] to get the following high-order PCP scheme

$$\overline{\mathbf{U}}_{ij}^{n+1} = \overline{\mathbf{U}}_{ij}^n - \frac{\Delta t^n}{\Delta x_i} (\widehat{\mathbf{F}}_{i+\frac{1}{2},j}^{\text{PCP}} - \widehat{\mathbf{F}}_{i-\frac{1}{2},j}^{\text{PCP}}) - \frac{\Delta t^n}{\Delta y_j} (\widehat{\mathbf{G}}_{i,j+\frac{1}{2}}^{\text{PCP}} - \widehat{\mathbf{G}}_{i,j-\frac{1}{2}}^{\text{PCP}}), \quad (3.16)$$

where

$$\widehat{\mathbf{F}}_{i\pm\frac{1}{2},j}^{\text{PCP}} = (1 - \theta_{i\pm\frac{1}{2},j}^x) \widehat{\mathbf{F}}_{i\pm\frac{1}{2},j}^{\text{low}} + \theta_{i\pm\frac{1}{2},j}^x \widehat{\mathbf{F}}_{i\pm\frac{1}{2},j}^{\text{high}}, \quad (3.17)$$

$$\widehat{\mathbf{G}}_{i,j\pm\frac{1}{2}}^{\text{PCP}} = (1 - \theta_{i,j\pm\frac{1}{2}}^y) \widehat{\mathbf{G}}_{i,j\pm\frac{1}{2}}^{\text{low}} + \theta_{i,j\pm\frac{1}{2}}^y \widehat{\mathbf{G}}_{i,j\pm\frac{1}{2}}^{\text{high}}, \quad (3.18)$$

with

$$\begin{aligned}\widehat{\mathbf{F}}_{i+\frac{1}{2},j}^{\text{low}} &= \frac{1}{2} \left(\mathbf{F}(\overline{\mathbf{U}}_{ij}^n) + \mathbf{F}(\overline{\mathbf{U}}_{i+1,j}^n) - \alpha_{i+\frac{1}{2},j}^n (\overline{\mathbf{U}}_{i+1,j}^n - \overline{\mathbf{U}}_{ij}^n) \right), \\ \widehat{\mathbf{G}}_{i,j+\frac{1}{2}}^{\text{low}} &= \frac{1}{2} \left(\mathbf{G}(\overline{\mathbf{U}}_{ij}^n) + \mathbf{G}(\overline{\mathbf{U}}_{i,j+1}^n) - \beta_{i,j+\frac{1}{2}}^n (\overline{\mathbf{U}}_{i,j+1}^n - \overline{\mathbf{U}}_{ij}^n) \right),\end{aligned}$$

and $\alpha_{i+\frac{1}{2},j}^n = \max\{\varrho^x(\overline{\mathbf{U}}_{i+1,j}^n), \varrho^x(\overline{\mathbf{U}}_{i,j}^n)\}$, $\beta_{i,j+\frac{1}{2}}^n = \max\{\varrho^y(\overline{\mathbf{U}}_{i,j+1}^n), \varrho^y(\overline{\mathbf{U}}_{i,j}^n)\}$. Here ϱ^x and ϱ^y are the spectral radii of the Jacobian matrices $\partial\mathbf{F}/\partial\mathbf{U}$ and $\partial\mathbf{G}/\partial\mathbf{U}$, respectively, $\theta_{i\pm\frac{1}{2},j}^x$ and $\theta_{i,j\pm\frac{1}{2}}^y$ are the PCP flux limiters defined below for $\widehat{\mathbf{F}}$ and $\widehat{\mathbf{G}}$, respectively.

If assuming $\overline{\mathbf{U}}_{ij}^n \in \mathcal{G}$ for any i, j , and the CFL-type condition

$$\Delta t^n \leq \frac{1}{4} \min_{i,j} \left(\frac{\Delta x_i}{\alpha_{i+\frac{1}{2},j}^n}, \frac{\Delta y_j}{\beta_{i,j+\frac{1}{2}}^n} \right), \quad (3.19)$$

then using the properties of \mathcal{G} in Lemma 1.2 yields

$$\mathbf{U}_{ij}^{\pm, \text{low}} := \bar{\mathbf{U}}_{ij}^n \mp \frac{4\Delta t^n}{\Delta x_i} \widehat{\mathbf{F}}_{i\pm\frac{1}{2},j}^{\text{low}} \in \mathcal{G}, \quad \tilde{\mathbf{U}}_{ij}^{\pm, \text{low}} := \bar{\mathbf{U}}_{ij}^n \mp \frac{4\Delta t^n}{\Delta y_j} \widehat{\mathbf{G}}_{i,j\pm\frac{1}{2}}^{\text{low}} \in \mathcal{G}.$$

Define

$$\mathbf{U}_{ij}^{\pm, \text{high}} := \bar{\mathbf{U}}_{ij}^n \mp \frac{4\Delta t^n}{\Delta x_i} \widehat{\mathbf{F}}_{i\pm\frac{1}{2},j}^{\text{high}}, \quad \tilde{\mathbf{U}}_{ij}^{\pm, \text{high}} := \bar{\mathbf{U}}_{ij}^n \mp \frac{4\Delta t^n}{\Delta y_j} \widehat{\mathbf{G}}_{i,j\pm\frac{1}{2}}^{\text{high}},$$

and introduce two small positive numbers ε_D and ε_q such that $D(\mathbf{U}_{ij}^{\pm, \text{low}}) \geq \varepsilon_D > 0$, $D(\tilde{\mathbf{U}}_{ij}^{\pm, \text{low}}) \geq \varepsilon_D > 0$, $q(\mathbf{U}_{ij}^{\pm, \text{low}}) \geq \varepsilon_q > 0$, $q(\tilde{\mathbf{U}}_{ij}^{\pm, \text{low}}) \geq \varepsilon_q > 0$. In our coming computations, $\varepsilon_D = \varepsilon_q = 10^{-14}$.

The PCP flux limiters $\theta_{i\pm\frac{1}{2},j}^x$ and $\theta_{i,j\pm\frac{1}{2}}^y$ are defined as follows.

(i) Enforce the positivity of the mass density $D(\mathbf{U})$. For each i and j , define

$$\theta_{i+\frac{1}{2},j}^{D,x,\pm} = \begin{cases} (D_{i+\frac{1}{2}\mp\frac{1}{2},j}^{\pm, \text{low}} - \varepsilon_D) / (D_{i+\frac{1}{2}\mp\frac{1}{2},j}^{\pm, \text{low}} - D_{i+\frac{1}{2}\mp\frac{1}{2},j}^{\pm, \text{high}}), & \text{if } D_{i+\frac{1}{2}\mp\frac{1}{2},j}^{\pm, \text{high}} < \varepsilon_D, \\ 1, & \text{otherwise,} \end{cases}$$

$$\theta_{i,j+\frac{1}{2}}^{D,y,\pm} = \begin{cases} (\tilde{D}_{i,j+\frac{1}{2}\mp\frac{1}{2}}^{\pm, \text{low}} - \varepsilon_D) / (\tilde{D}_{i,j+\frac{1}{2}\mp\frac{1}{2}}^{\pm, \text{low}} - \tilde{D}_{i,j+\frac{1}{2}\mp\frac{1}{2}}^{\pm, \text{high}}), & \text{if } \tilde{D}_{i,j+\frac{1}{2}\mp\frac{1}{2}}^{\pm, \text{high}} < \varepsilon_D, \\ 1, & \text{otherwise,} \end{cases}$$

and limit

$$\left\{ \widehat{\mathbf{F}}_{i+\frac{1}{2},j}^D \right\}_k = \begin{cases} (1 - \theta_{i+\frac{1}{2},j}^{D,x,+}) \left\{ \widehat{\mathbf{F}}_{i+\frac{1}{2},j}^{\text{low}} \right\}_k + \theta_{i+\frac{1}{2},j}^{D,x,-} \left\{ \widehat{\mathbf{F}}_{i+\frac{1}{2},j}^{\text{high}} \right\}_k, & k = 1, \\ \left\{ \widehat{\mathbf{F}}_{i+\frac{1}{2},j}^{\text{high}} \right\}_k, & k > 1, \end{cases} \quad (3.20)$$

$$\left\{ \widehat{\mathbf{G}}_{i,j+\frac{1}{2}}^D \right\}_k = \begin{cases} (1 - \theta_{i,j+\frac{1}{2}}^{D,y,+}) \left\{ \widehat{\mathbf{G}}_{i,j+\frac{1}{2}}^{\text{low}} \right\}_k + \theta_{i,j+\frac{1}{2}}^{D,y,-} \left\{ \widehat{\mathbf{G}}_{i,j+\frac{1}{2}}^{\text{high}} \right\}_k, & k = 1, \\ \left\{ \widehat{\mathbf{G}}_{i,j+\frac{1}{2}}^{\text{high}} \right\}_k, & k > 1, \end{cases} \quad (3.21)$$

where $\theta_{i+\frac{1}{2},j}^{D,x} = \min\{\theta_{i+\frac{1}{2},j}^{D,x,+}, \theta_{i+\frac{1}{2},j}^{D,x,-}\}$, $\theta_{i,j+\frac{1}{2}}^{D,y} = \min\{\theta_{i,j+\frac{1}{2}}^{D,y,+}, \theta_{i,j+\frac{1}{2}}^{D,y,-}\}$, and $\left\{ \widehat{\mathbf{F}}_{i+\frac{1}{2},j} \right\}_k$, $\left\{ \widehat{\mathbf{G}}_{i,j+\frac{1}{2}} \right\}_k$ are the k -th components of $\widehat{\mathbf{F}}_{i+\frac{1}{2},j}$ and $\widehat{\mathbf{G}}_{i,j+\frac{1}{2}}$ respectively.

(ii) Enforce the positivity of the term $q(\mathbf{U}) = E - \sqrt{D^2 + |\mathbf{m}|^2}$. For each i, j , compute

$$\theta_{i+\frac{1}{2},j}^{q,x,\pm} = \begin{cases} (q(\mathbf{U}_{i+\frac{1}{2}\mp\frac{1}{2},j}^{\pm, \text{low}}) - \varepsilon_q) / (q(\mathbf{U}_{i+\frac{1}{2}\mp\frac{1}{2},j}^{\pm, \text{low}}) - q(\mathbf{U}_{i+\frac{1}{2}\mp\frac{1}{2},j}^{\pm, \text{D}})), & \text{if } q(\mathbf{U}_{i+\frac{1}{2}\mp\frac{1}{2},j}^{\pm, \text{D}}) < \varepsilon_q, \\ 1, & \text{otherwise,} \end{cases}$$

$$\theta_{i,j+\frac{1}{2}}^{q,y,\pm} = \begin{cases} (q(\tilde{\mathbf{U}}_{i,j+\frac{1}{2}\mp\frac{1}{2}}^{\pm, \text{low}}) - \varepsilon_q) / (q(\tilde{\mathbf{U}}_{i,j+\frac{1}{2}\mp\frac{1}{2}}^{\pm, \text{low}}) - q(\tilde{\mathbf{U}}_{i,j+\frac{1}{2}\mp\frac{1}{2}}^{\pm, \text{D}})), & \text{if } q(\tilde{\mathbf{U}}_{i,j+\frac{1}{2}\mp\frac{1}{2}}^{\pm, \text{D}}) < \varepsilon_q, \\ 1, & \text{otherwise,} \end{cases}$$

and then limit the numerical fluxes as

$$\widehat{\mathbf{F}}_{i+\frac{1}{2},j}^{\text{PCP}} = (1 - \theta_{i+\frac{1}{2},j}^{q,x,+}) \widehat{\mathbf{F}}_{i+\frac{1}{2},j}^{\text{low}} + \theta_{i+\frac{1}{2},j}^{q,x,-} \widehat{\mathbf{F}}_{i+\frac{1}{2},j}^{\text{D}}, \quad (3.22)$$

$$\widehat{\mathbf{G}}_{i,j+\frac{1}{2}}^{\text{PCP}} = (1 - \theta_{i,j+\frac{1}{2}}^{q,y}) \widehat{\mathbf{G}}_{i,j+\frac{1}{2}}^{\text{low}} + \theta_{i,j+\frac{1}{2}}^{q,y} \widehat{\mathbf{G}}_{i,j+\frac{1}{2}}^{\text{D}}, \quad (3.23)$$

where $\theta_{i+\frac{1}{2},j}^{q,x} = \min\{\theta_{i+\frac{1}{2},j}^{q,x,+}, \theta_{i+\frac{1}{2},j}^{q,x,-}\}$ and $\theta_{i,j+\frac{1}{2}}^{q,y} = \min\{\theta_{i,j+\frac{1}{2}}^{q,y,+}, \theta_{i,j+\frac{1}{2}}^{q,y,-}\}$.

(iii) Define $\theta_{i\pm\frac{1}{2},j}^x := \theta_{i\pm\frac{1}{2},j}^{D,x} \theta_{i\pm\frac{1}{2},j}^{q,x}$ and $\theta_{i,j\pm\frac{1}{2}}^y := \theta_{i,j\pm\frac{1}{2}}^{D,y} \theta_{i,j\pm\frac{1}{2}}^{q,y}$.

It is not difficult to prove that the scheme (3.16) is consistent with the 2D RHD equations in (1.1) and also is PCP, when $\overline{\mathbf{U}}_{ij}^n \in \mathcal{G}$ and a suitable time stepsize is given (see Theorem 3.2). Furthermore, we also remark that such PCP limiter does not destroy the original high order accuracy in the smooth region, more details can be seen in [45].

Theorem 3.2. *Under the time step size restriction in (3.19), if $\mathbf{U}_{ij}^{\pm,\text{low}}, \widetilde{\mathbf{U}}_{ij}^{\pm,\text{low}} \in \mathcal{G}$ for all i, j , and the wave speeds are estimated in (2.1), then for the high-order finite volume scheme (3.15) we have*

$$\overline{\mathbf{U}}_{ij}^{n+1} = \frac{1}{4} \left(\mathbf{U}_{ij}^{+,\text{PCP}} + \mathbf{U}_{ij}^{-,\text{PCP}} + \widetilde{\mathbf{U}}_{ij}^{+,\text{PCP}} + \widetilde{\mathbf{U}}_{ij}^{-,\text{PCP}} \right) \in \mathcal{G}, \quad \forall i, j,$$

where

$$\mathbf{U}_{ij}^{\pm,\text{PCP}} = \overline{\mathbf{U}}_{ij}^n \mp \frac{4\Delta t^n}{\Delta x_i} \widehat{\mathbf{F}}_{i\pm\frac{1}{2},j}^{\text{PCP}}, \quad \widetilde{\mathbf{U}}_{ij}^{\pm,\text{PCP}} = \overline{\mathbf{U}}_{ij}^n \mp \frac{4\Delta t^n}{\Delta y_j} \widehat{\mathbf{G}}_{i,j\pm\frac{1}{2}}^{\text{PCP}}.$$

Proof. Since $\overline{\mathbf{U}}_{ij}^{n+1}$ is a convex combination of four terms $\mathbf{U}_{ij}^{+,\text{PCP}}, \mathbf{U}_{ij}^{-,\text{PCP}}, \widetilde{\mathbf{U}}_{ij}^{+,\text{PCP}}, \widetilde{\mathbf{U}}_{ij}^{-,\text{PCP}}$, a sufficient condition for $\overline{\mathbf{U}}_{ij}^{n+1} \in \mathcal{G}$ is that each term belongs to the admissible set \mathcal{G} due to the convexity of \mathcal{G} , see Lemma 1.1. Without loss of generality, we here just provide the proof for $\mathbf{U}_{ij}^{\pm,\text{PCP}} \in \mathcal{G}$ and similar analysis can be applied on $\widetilde{\mathbf{U}}_{ij}^{\pm,\text{PCP}}$.

With the assumption and the above PCP flux limiter, we know that $0 \leq \theta_{i+\frac{1}{2},j}^{D,x} \leq 1, 0 \leq \theta_{i+\frac{1}{2},j}^{q,x} \leq 1$ and there exist two small positive numbers ε_D and ε_q such that $D_{ij}^{\pm,\text{low}} \geq \varepsilon_D > 0, q(\mathbf{U}_{ij}^{\pm,\text{low}}) \geq \varepsilon_q > 0$.

Combining (3.20) and (3.22) gets

$$\left\{ \widehat{\mathbf{F}}_{i\pm\frac{1}{2},j}^{\text{PCP}} \right\}_1 = (1 - \theta_{i\pm\frac{1}{2},j}^x) \left\{ \widehat{\mathbf{F}}_{i\pm\frac{1}{2},j}^{\text{low}} \right\}_1 + \theta_{i\pm\frac{1}{2},j}^x \left\{ \widehat{\mathbf{F}}_{i\pm\frac{1}{2},j}^{\text{high}} \right\}_1,$$

and then

$$D_{ij}^{\pm,\text{PCP}} = (1 - \theta_{i\pm\frac{1}{2},j}^x) D_{ij}^{\pm,\text{low}} + \theta_{i\pm\frac{1}{2},j}^x D_{ij}^{\pm,\text{high}}.$$

According to the definitions of $\theta_{i\pm\frac{1}{2},j}^x$ and $\theta_{i\pm\frac{1}{2},j}^{D,x,\pm}$, one has

$$0 < \theta_{i\pm\frac{1}{2},j}^x \leq \theta_{i\pm\frac{1}{2},j}^{D,x} \leq \theta_{i\pm\frac{1}{2},j}^{D,x,\pm} \leq 1,$$

and

$$(1 - \theta_{i\pm\frac{1}{2},j}^{D,x,\pm}) D_{ij}^{\pm,\text{low}} + \theta_{i\pm\frac{1}{2},j}^{D,x,\pm} D_{ij}^{\pm,\text{high}} \geq \varepsilon_D > 0,$$

which implies

$$\begin{aligned} D_{ij}^{\pm,\text{PCP}} &= (1 - \theta_{i\pm\frac{1}{2},j}^x) D_{ij}^{\pm,\text{low}} + \theta_{i\pm\frac{1}{2},j}^x D_{ij}^{\pm,\text{high}} \\ &= \frac{\theta_{i\pm\frac{1}{2},j}^x}{\theta_{i\pm\frac{1}{2},j}^{D,x,\pm}} \left((1 - \theta_{i\pm\frac{1}{2},j}^{D,x,\pm}) D_{ij}^{\pm,\text{low}} + \theta_{i\pm\frac{1}{2},j}^{D,x,\pm} D_{ij}^{\pm,\text{high}} \right) + \left(1 - \frac{\theta_{i\pm\frac{1}{2},j}^x}{\theta_{i\pm\frac{1}{2},j}^{D,x,\pm}} \right) D_{ij}^{\pm,\text{low}} \\ &\geq \frac{\theta_{i\pm\frac{1}{2},j}^x}{\theta_{i\pm\frac{1}{2},j}^{D,x,\pm}} \varepsilon_D + \left(1 - \frac{\theta_{i\pm\frac{1}{2},j}^x}{\theta_{i\pm\frac{1}{2},j}^{D,x,\pm}} \right) \varepsilon_D = \varepsilon_D > 0. \end{aligned}$$

On the other hand, (3.22) gives

$$\mathbf{U}_{ij}^{\pm,\text{PCP}} = (1 - \theta_{i\pm\frac{1}{2},j}^{q,x}) \mathbf{U}_{ij}^{\pm,\text{low}} + \theta_{i\pm\frac{1}{2},j}^{q,x} \mathbf{U}_{ij}^{\pm,\text{D}},$$

and then

$$q(\mathbf{U}_{ij}^{\pm,\text{PCP}}) = q\left((1 - \theta_{i\pm\frac{1}{2},j}^{q,x}) \mathbf{U}_{ij}^{\pm,\text{low}} + \theta_{i\pm\frac{1}{2},j}^{q,x} \mathbf{U}_{ij}^{\pm,\text{D}}\right) \geq (1 - \theta_{i\pm\frac{1}{2},j}^{q,x}) q(\mathbf{U}_{ij}^{\pm,\text{low}}) + \theta_{i\pm\frac{1}{2},j}^{q,x} q(\mathbf{U}_{ij}^{\pm,\text{D}}),$$

since the function $q(\mathbf{U})$ is concave. Hence we obtain

$$\begin{aligned} q(\mathbf{U}_{ij}^{\pm,\text{PCP}}) &\geq (1 - \theta_{i\pm\frac{1}{2},j}^{q,x}) q(\mathbf{U}_{ij}^{\pm,\text{low}}) + \theta_{i\pm\frac{1}{2},j}^{q,x} q(\mathbf{U}_{ij}^{\pm,\text{D}}) \\ &= \frac{\theta_{i\pm\frac{1}{2},j}^{q,x}}{\theta_{i\pm\frac{1}{2},j}^{q,x,\pm}} \left((1 - \theta_{i\pm\frac{1}{2},j}^{q,x,\pm}) q(\mathbf{U}_{ij}^{\pm,\text{low}}) + \theta_{i\pm\frac{1}{2},j}^{q,x,\pm} q(\mathbf{U}_{ij}^{\pm,\text{D}}) \right) + \left(1 - \frac{\theta_{i\pm\frac{1}{2},j}^{q,x}}{\theta_{i\pm\frac{1}{2},j}^{q,x,\pm}} \right) q(\mathbf{U}_{ij}^{\pm,\text{low}}) \\ &\geq \frac{\theta_{i\pm\frac{1}{2},j}^{q,x}}{\theta_{i\pm\frac{1}{2},j}^{q,x,\pm}} \varepsilon_q + \left(1 - \frac{\theta_{i\pm\frac{1}{2},j}^{q,x}}{\theta_{i\pm\frac{1}{2},j}^{q,x,\pm}} \right) \varepsilon_q = \varepsilon_q > 0. \end{aligned}$$

Thus, $\mathbf{U}_{ij}^{\pm,\text{PCP}} \in \mathcal{G}$. The proof is completed. \square

Remark 3.2. In practice, the computation of the numerical fluxes $\widehat{\mathbf{F}}_{i+\frac{1}{2},j}^{\text{high}}$ and $\widehat{\mathbf{G}}_{i,j+\frac{1}{2}}^{\text{high}}$ needs that the reconstructed values $\mathbf{U}_{ij}^n(x_i^\alpha, y_{j+\frac{1}{2}})$ and $\mathbf{U}_{ij}^n(x_{i+\frac{1}{2}}, y_j^\beta)$ are in the admissible set \mathcal{G} . It may be enforced by using the PCP limiter similar to the above by replacing $\mathbf{U}_{ij}^{\pm,\text{high}}$ and $\widetilde{\mathbf{U}}_{ij}^{\pm,\text{high}}$, see [47, 23].

Remark 3.3. *In order to get a scheme of high order accuracy both in space and time, we replace the forward Euler time discretization in the PCP scheme (3.16) with an explicit third-order accurate SSP Runge-Kutta time discretization, which is still PCP under a suitable CFL-type condition and is implemented as follows:*

$$\begin{aligned}\bar{\mathbf{U}}_{ij}^{(1)} &= \bar{\mathbf{U}}_{ij}^n - \Delta t^n \mathcal{L}(\bar{\mathbf{U}}_{ij}^n), \\ \bar{\mathbf{U}}_{ij}^{(2)} &= \frac{3}{4}\bar{\mathbf{U}}_{ij}^n + \frac{1}{4}\left(\bar{\mathbf{U}}_{ij}^{(1)} - \Delta t^n \mathcal{L}(\bar{\mathbf{U}}_{ij}^{(1)})\right), \\ \bar{\mathbf{U}}_{ij}^{n+1} &= \frac{1}{3}\bar{\mathbf{U}}_{ij}^n + \frac{2}{3}\left(\bar{\mathbf{U}}_{ij}^{(2)} - \Delta t^n \mathcal{L}(\bar{\mathbf{U}}_{ij}^{(2)})\right),\end{aligned}$$

where

$$\mathcal{L}(\bar{\mathbf{U}}_{ij}) = \frac{1}{\Delta x_i}(\hat{\mathbf{F}}_{i+\frac{1}{2},j}^{\text{PCP}} - \hat{\mathbf{F}}_{i-\frac{1}{2},j}^{\text{PCP}}) + \frac{1}{\Delta y_j}(\hat{\mathbf{G}}_{i,j+\frac{1}{2}}^{\text{PCP}} - \hat{\mathbf{G}}_{i,j-\frac{1}{2}}^{\text{PCP}}).$$

4 Numerical tests

This section conducts several numerical experiments on the 2D ultra-relativistic RHD problems with large Lorentz factor, or strong discontinuities, or low rest-mass density or pressure, to verify the accuracy, robustness, and effectiveness of the present PCP schemes. It is worth remarking that those ultra-relativistic RHD problems seriously challenge the numerical schemes. Unless otherwise stated, all the computations are restricted to the EOS (1.3) with the adiabatic index $\Gamma = 5/3$, and the time step size Δt^n determined by (3.3) with the CFL number $\sigma = 0.45$. Moreover, in our computations, we apply the fifth-order WENO reconstruction [37] and replace Δt^n with $(\Delta t^n)^{5/3}$ to match the spacial accuracy in Examples 4.2 and 4.3.

Example 4.1. We first construct a explosion problem to test the multi-dimensionality of our scheme by referring to that in [3]. Initially, the rest fluid with a unit rest-mass density is in the domain $\Omega = [-0.5, 0.5]^2$. The pressure is set as 20 inside a circle of radius 1/10, while a smaller pressure of 0.1 is given all over outside the circle. Figure 4.1 plots the contours and cross sections along y -axis and $y = x$ of the rest-mass density at $t = 0.1$ obtained by using our first-order PCP scheme with the multidimensional Riemann solver, i.e. (3.1) with (3.6)-(3.7), on the mesh of 64×64 uniform cells. For a comparison, -eps-converted-to.pdf 4.2 gives the

numerical solutions obtained by using corresponding scheme with the 1D Riemann solver, i.e. (3.1) with $\widehat{\mathbf{F}}_{i+\frac{1}{2},j} = \mathbf{F}_{i+\frac{1}{2},j}^{**}$ and $\widehat{\mathbf{G}}_{i,j+\frac{1}{2}} = \mathbf{G}_{i,j+\frac{1}{2}}^{**}$. It can be clearly seen from them that the results obtained by our scheme with the 2D Riemann solver preserve the spherical symmetry better.

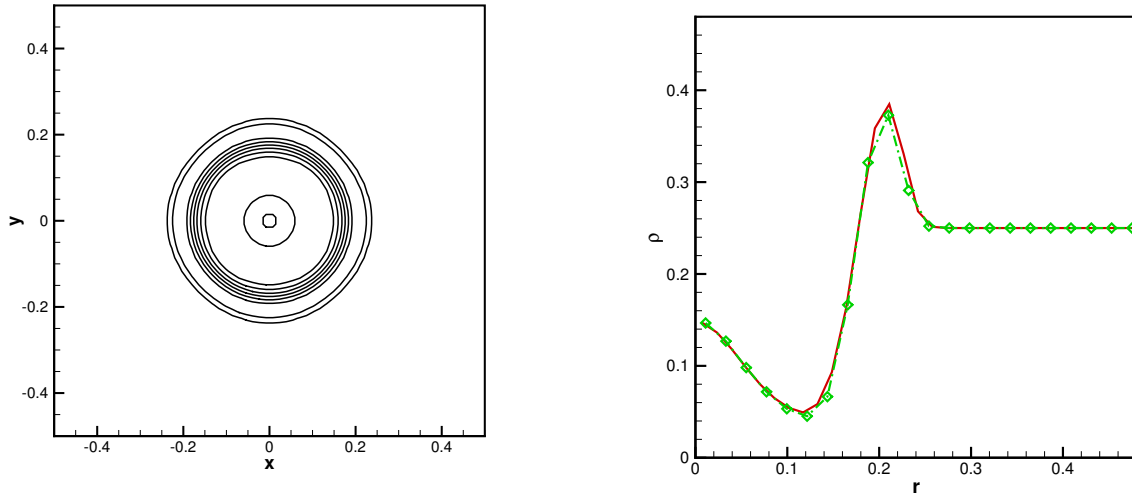


Figure 4.1: Example 4.1: The rest-mass density at $t = 0.1$ obtained from our first-order PCP scheme with the 2D HLL Riemann solver. Left: The contours with eight equally spaced contour lines; right: the cross sections of ρ at y -axis (solid line) and $y = x$ (dashed line with the symbol “ \diamond ”).

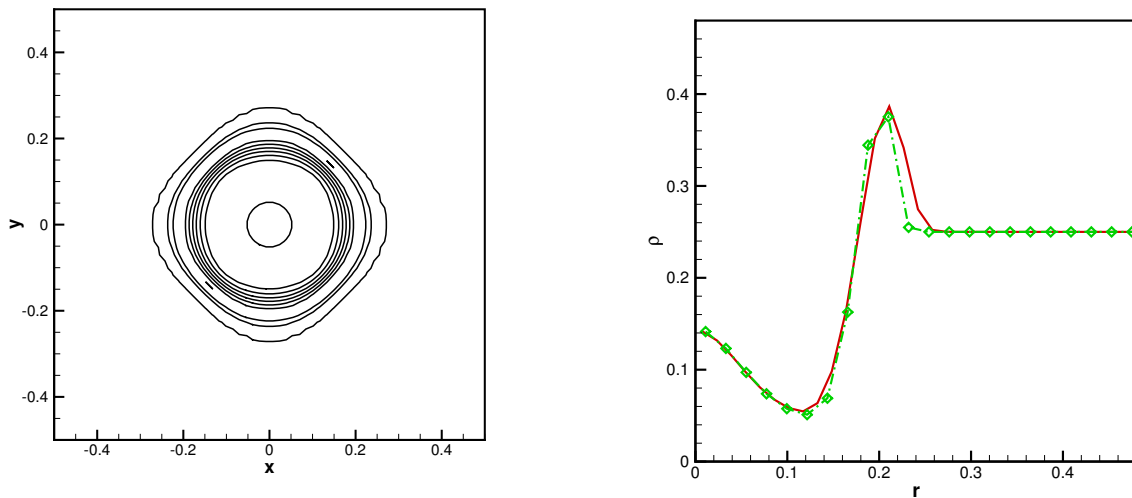


Figure 4.2: Same as Figure 4.1, except for the 1D HLL Riemann solver.

Example 4.2 (Sine wave propagation [47]). This problem is used to test the accuracy of our PCP finite volume schemes. Its exact solution is

$$(\rho, u, v, p)(x, y, t) = (1 + 0.99999 \sin(2\pi(x + y - 0.99\sqrt{2}t)), 0.99/\sqrt{2}, 0.99/\sqrt{2}, 0.01), t \geq 0$$

which describes an RHD sine wave propagating periodically in the domain $\Omega = [0, 1]^2$ at an angle 45° with the x -axis. The computational domain is divided into $N \times N$ uniform cells, and the periodic boundary conditions are specified on the boundary of Ω . Tables 4.1 and 4.2 list the ℓ^1 , ℓ^2 and ℓ^∞ errors at $t = 0.1$ and orders of convergence obtained from our first-order and fifth-order multidimensional PCP schemes respectively. The results show the expected PCP performance. Table 4.2 also lists the proportions of the PCP limited cells at all time levels, denoted by Θ_N^1 (scaling PCP limiter) and Θ_N^2 (PCP flux limiter). It can be observed that the PCP limiter has been performed in the fifth-order accurate scheme because of the low density, and the usage of the limiter does not destroy the higher-order accuracy.

Table 4.1: Example 4.2: Errors and orders of convergence for the mass density at $t = 0.1$ obtained by using the first-order PCP scheme with the mesh of $N \times N$ uniform cells.

N	ℓ^1 error	ℓ^1 order	ℓ^2 error	ℓ^2 order	ℓ^∞ error	ℓ^∞ order
20	3.91E-01	—	4.36E-01	—	6.16E-01	—
40	1.92E-01	1.03	2.13E-01	1.03	3.01E-01	1.03
80	9.49E-02	1.02	1.05E-01	1.02	1.49E-01	1.01
160	4.76E-02	1.00	5.28E-02	1.00	7.47E-02	1.00
320	2.38E-02	1.00	2.65E-02	1.00	3.74E-02	1.00

Table 4.2: Example 4.2: Same as Table 4.1, except for the fifth-order PCP scheme.

N	ℓ^1 error	ℓ^1 order	ℓ^2 error	ℓ^2 order	ℓ^∞ error	ℓ^∞ order	Θ_N^1 (%)	Θ_N^2 (%)
10	3.70E-02	—	4.08E-02	—	6.18E-02	—	36.18	0.00
20	1.37E-03	4.75	1.59E-03	4.68	3.07E-03	4.33	12.36	0.00
40	3.96E-05	5.12	4.64E-05	5.10	9.12E-05	5.07	1.85	0.00
80	1.19E-06	5.05	1.38E-06	5.07	2.87E-06	4.99	0.00	0.00
160	3.64E-08	5.03	4.15E-08	5.06	8.56E-08	5.07	0.00	0.00

Example 4.3 (Relativistic isentropic vortex). It is a 2D relativistic isentropic vortex problem constructed first in [23], where the vortex in the space-time coordinate system (x, y, t) moves with a constant speed of magnitude w in $(-1, -1)$ direction. The time-dependent solution (ρ, u, v, p) at time $t \geq 0$ is given as follows

$$\begin{aligned}\rho &= (1 - \alpha e^{1-r^2})^{\frac{1}{\Gamma-1}}, & p &= \rho^\Gamma, \\ u &= \frac{1}{1 - \frac{w(u_0+v_0)}{\sqrt{2}}} \left[\frac{u_0}{\gamma} - \frac{w}{\sqrt{2}} + \frac{\gamma w^2}{2(\gamma+1)}(u_0 + v_0) \right], \\ v &= \frac{1}{1 - \frac{w(u_0+v_0)}{\sqrt{2}}} \left[\frac{v_0}{\gamma} - \frac{w}{\sqrt{2}} + \frac{\gamma w^2}{2(\gamma+1)}(u_0 + v_0) \right],\end{aligned}$$

where

$$\begin{aligned}\gamma &= \frac{1}{\sqrt{1-w^2}}, & r &= \sqrt{x_0^2 + y_0^2}, & (u_0, v_0) &= (-y_0, x_0)f, \\ \alpha &= \frac{(\Gamma-1)}{8\Gamma\pi^2}\epsilon^2, & \beta &= \frac{2\Gamma\alpha e^{1-r^2}}{2\Gamma-1-\Gamma\alpha e^{1-r^2}}, & f &= \sqrt{\frac{\beta}{1+\beta r^2}}, \\ x_0 &= x + \frac{\gamma-1}{2}(x+y) + \frac{\gamma tw}{\sqrt{2}}, & y_0 &= y + \frac{\gamma-1}{2}(x+y) + \frac{\gamma tw}{\sqrt{2}}.\end{aligned}$$

Our computations are performed in the domain $\Omega = [-6, 6]^2$ with the adiabatic index $\Gamma = 1.4$, $w = 0.5\sqrt{2}$, the vortex strength $\epsilon = 10.0828$, and the periodic boundary conditions. In this case, the lowest density and lowest pressure are 7.83×10^{-15} and 1.78×10^{-20} , respectively.

Tables 4.3 and 4.4 give the errors of the rest-mass density at $t = 1$ and the orders of convergence obtained from our first- and fifth-order PCP schemes respectively. It is clear to see that our multidimensional PCP schemes achieves the expected accuracy and preserves the positivity of the density and pressure simultaneously. Also the proportions of the PCP limited cells at all time levels, denoted by Θ_N^1 (scaling PCP limiter) and Θ_N^2 (PCP flux limiter), are listed to show that the PCP limiter is indeed used to preserve the admissibility of numerical solutions.

Table 4.3: Example 4.3: Errors and orders of convergence for mass density at $t = 1$ obtained by using the first-order PCP scheme with the mesh of $N \times N$ uniform cells.

N	ℓ^1 error	ℓ^1 order	ℓ^2 error	ℓ^2 order	ℓ^∞ error	ℓ^∞ order
20	2.48E+00	—	7.41E-01	—	5.54E-01	—
40	1.63E+00	0.60	4.90E-01	0.60	3.61E-01	0.62
80	9.42E-01	0.80	2.91E-01	0.75	2.19E-01	0.72
160	5.12E-01	0.88	1.63E-01	0.84	1.30E-01	0.76
320	2.68E-01	0.93	8.66E-02	0.91	7.14E-02	0.86

Table 4.4: Example 4.3: Same as Table 4.3, except for the fifth-order PCP scheme.

N	ℓ^1 error	ℓ^1 order	ℓ^2 error	ℓ^2 order	ℓ^∞ error	ℓ^∞ order	Θ_N^1 (%)	Θ_N^2 (%)
20	9.12E-01	—	2.88E-01	—	2.37E-01	—	3.21	3.82
40	1.63E-01	2.49	7.60E-02	1.92	9.66E-02	1.30	1.53	1.85
80	8.66E-03	4.23	4.56E-03	4.06	1.19E-02	3.03	5.13E-01	7.13E-02
160	3.22E-04	4.75	1.64E-04	4.80	4.36E-04	4.77	2.34E-02	2.57E-04
320	1.12E-05	4.84	6.12E-06	4.74	1.84E-05	4.56	7.74E-04	2.77E-05
640	3.58E-07	4.97	1.95E-07	4.97	7.86E-07	4.55	9.40E-05	2.04E-06

Example 4.4 (Riemann problem I). This example solves the 2D Riemann problem [45]. The initial data are given by

$$(\rho, u, v, p)(x, y, 0) = \begin{cases} (0.1, 0, 0, 0.01), & x > 0.5, y > 0.5, \\ (0.1, 0.99, 0, 1), & x < 0.5, y > 0.5, \\ (0.5, 0, 0, 1), & x < 0.5, y < 0.5, \\ (0.1, 0, 0.99, 1), & x > 0.5, y < 0.5, \end{cases}$$

where both the left and bottom discontinuities are contact discontinuities with a jump in the transverse velocity, while both the right and top discontinuities are not simple waves.

The computational domain Ω is taken as $[0, 1]^2$ and is divided into a uniform mesh with 400×400 cells. -eps-converted-to.pdf 4.3 and 4.4 display the contours of the rest-mass density logarithm $\ln \rho$ and the pressure logarithm $\ln p$ at $t = 0.4$ obtained by using the first- and the

fifth-order PCP schemes respectively. We can see that the four initial discontinuities interact each other and form two reflected curved shock waves, an elongated jet-like spike. It is worth mentioning that a non-PCP scheme fails when simulating this problem. Figure 4.5 also presents the cross sections of the numerical approximations along the line $y = x$ with 400×400 uniform mesh for the fifth-order PCP scheme and the same mesh, finer meshes of 800×800 and 1200×1200 for the first-order PCP scheme. It is obvious that the fifth-order scheme can capture the discontinuities better than the first-order scheme. Moreover, we count the PCP limited cells at each time level and the proportions are plotted in the Figure 4.6, from which one can clearly conclude that for the method without PCP property the simulation of this problem may fail.

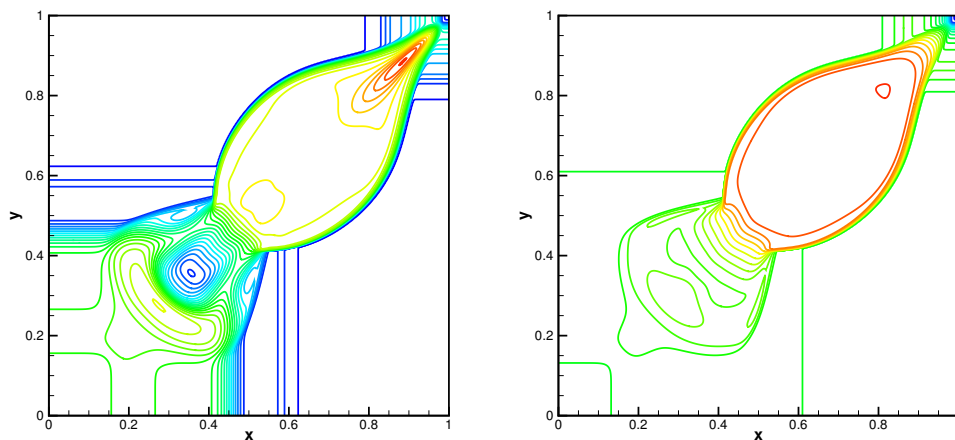


Figure 4.3: Example 4.4: The contours of the density logarithm $\ln \rho$ (left) and the pressure logarithm $\ln p$ (right) at $t = 0.4$ obtained from the first-order PCP scheme. 25 equally spaced contour lines are used.

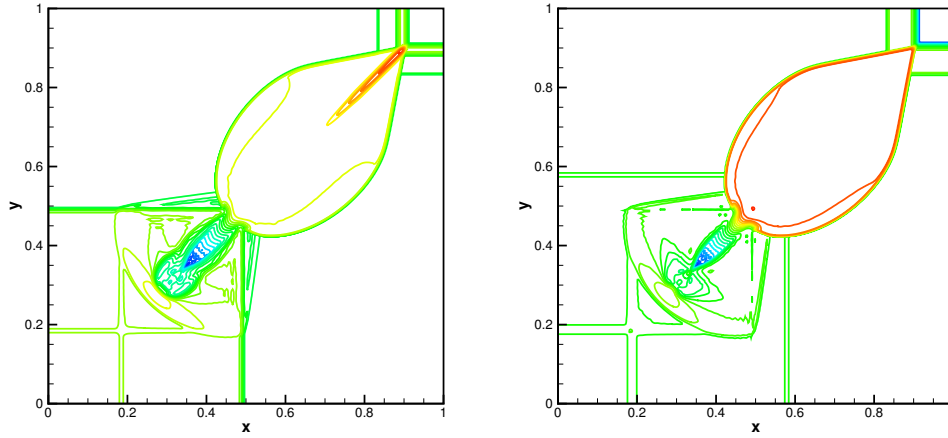


Figure 4.4: Example 4.4: Same as Figure 4.3 except for the fifth-order PCP scheme.

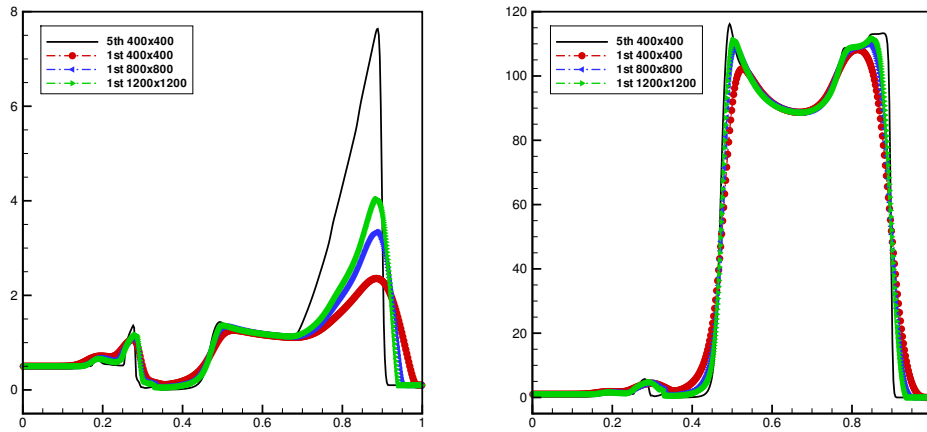


Figure 4.5: Example 4.4: Comparison of the cross sections of the numerical solutions at the line $y = x$ and $t = 0.4$ in the closed interval $x \in [0, 1]$ for different meshes and schemes. Left: the rest-mass density ρ ; Right: the pressure p .

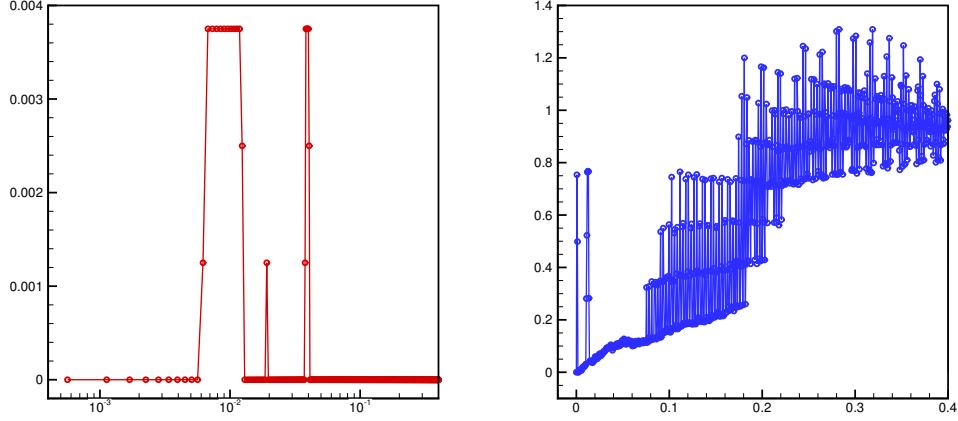


Figure 4.6: Example 4.4: Proportions of the PCP limited cells at each time level. Left: scaling PCP limiter; Right: PCP flux limiter.

Example 4.5 (Riemann problem II [45]). The initial data of the second Riemann problem are

$$(\rho, u, v, p)(x, y, 0) = \begin{cases} (0.1, 0, 0, 20), & x > 0.5, y > 0.5, \\ (\tilde{\rho}, \tilde{u}, 0, 0.05), & x < 0.5, y > 0.5, \\ (0.01, 0, 0, 0.05), & x < 0.5, y < 0.5, \\ (\tilde{\rho}, 0, \tilde{u}, 0.05), & x > 0.5, y < 0.5, \end{cases}$$

with $\tilde{\rho} = 0.00414329639576$, $\tilde{u} = 0.9946418833556542$ and the computational domain $\Omega = [0, 1]^2$. In this problem, the left and lower initial discontinuities are contact discontinuities, while the upper and right are shock waves with a speed of -0.66525606186639 . As the time increases, the maximal value of the fluid velocity becomes very large and close to the speed of light, which leads to the numerical simulation more challenging. Figures 4.7 and 4.8 show the contours of the rest-mass density logarithm $\ln \rho$ and the pressure logarithm $\ln p$ at $t = 0.4$ obtained by using the first- and fifth-order PCP schemes on the uniform mesh of 400×400 cells, respectively. The interaction of four initial discontinuities results in the distortion of the initial shock waves and the formation of a “mushroom cloud” starting from the point $(0.5, 0.5)$ and expanding to the left bottom region. We also compare the numerical solutions obtained from the first- and high-order schemes in Figure 4.9, which displays the plots of the rest-mass logarithm $\ln \rho$ and the pressure logarithm $\ln p$ along the line $y = x$. We can see that the fifth-

order PCP scheme gets better resolution for discontinuities than the first-order scheme even on a finer mesh. Furthermore, we also want to remark that a PCP scheme is necessary to simulate this problem since the PCP flux limiter and scaling PCP limiter are indeed used to preserve the physical-constraints property, see Figure 4.10.

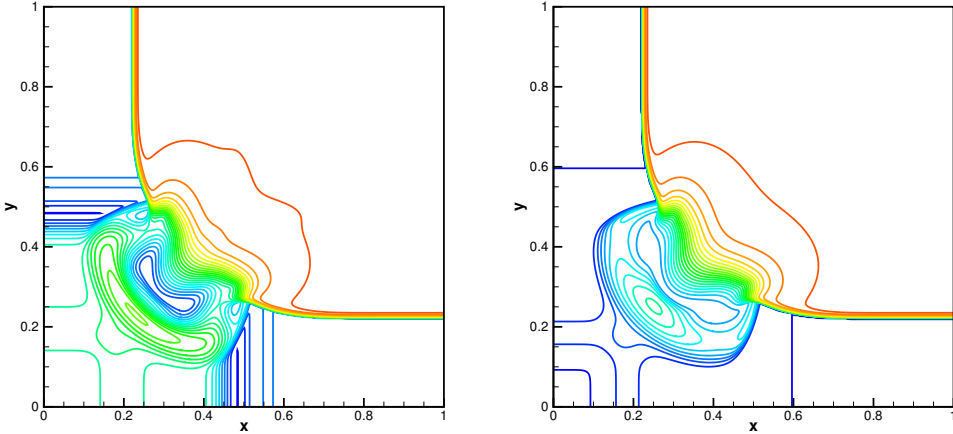


Figure 4.7: Example 4.5: The contours of the density logarithm $\ln \rho$ (left) and the pressure logarithm $\ln p$ (right) at $t = 0.4$ obtained from the first-order PCP scheme. 25 equally spaced contour lines are shown.

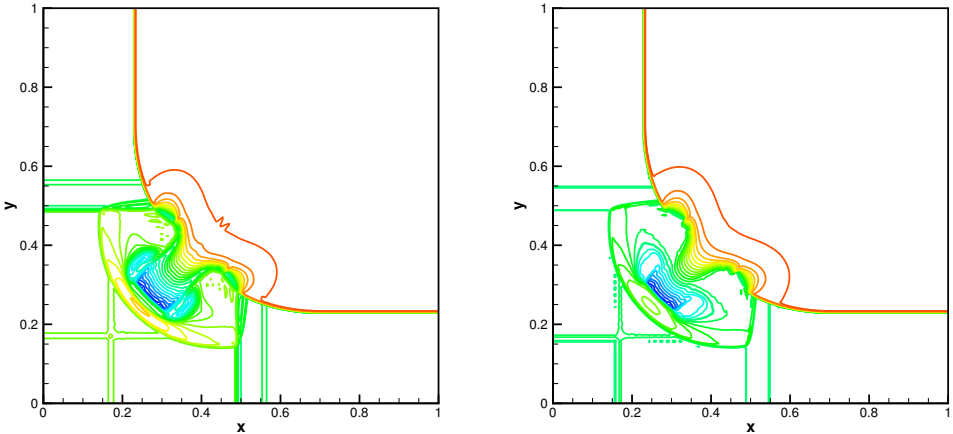


Figure 4.8: Example 4.5: Same as Figure 4.7 except for the fifth-order PCP scheme.

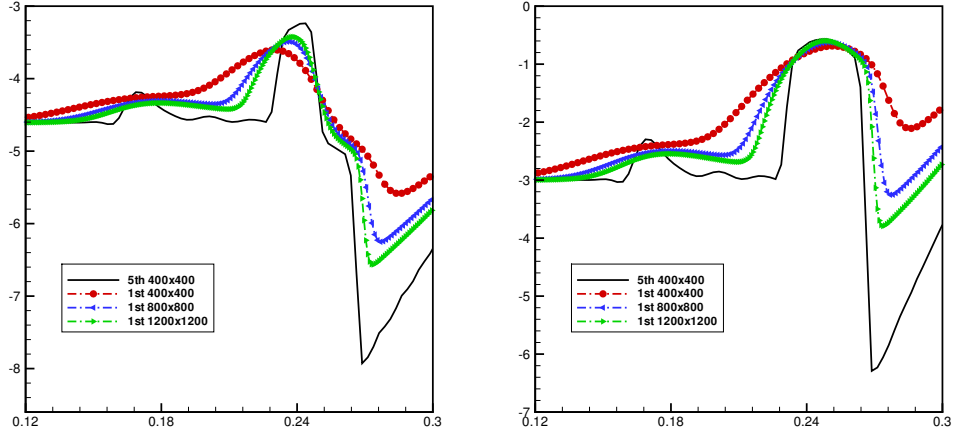


Figure 4.9: Example 4.5: Comparison of the cross sections of the numerical solutions at the line $y = x$ and $t = 0.4$ for different meshes and schemes in the closed interval $x \in [0.12, 0.3]$. Left: the rest-mass density logarithm $\ln \rho$; Right: the pressure logarithm $\ln p$.

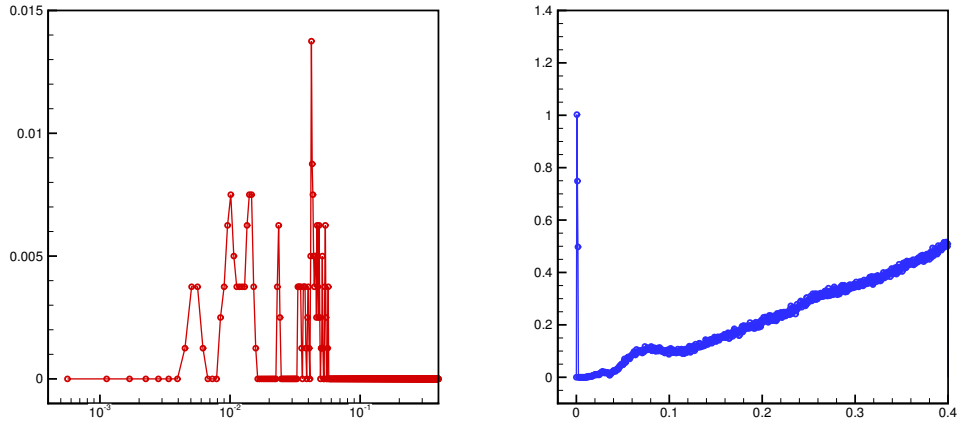


Figure 4.10: Example 4.5: Proportions of the PCP limited cells at each time level. Left: scaling PCP limiter; Right: PCP flux limiter.

Example 4.6 (Relativistic jets). The last example is to simulate the high-speed relativistic jet flows, which are ubiquitous in the extragalactic radio sources associated with the active galactic nuclei, and the most compelling case for a special relativistic phenomenon [47]. The simulation of such jet flows is full of challenge since there may appear the strong relativistic shock waves, shear waves, interface instabilities, and ultra-relativistic regions, as well as high speed jets etc.

Here we consider a pressure-matched hot jet model, in which the relativistic effects from the large beam internal energies are important and comparable to the effects from the fluid

velocity near the speed of light because the classical beam Mach number $M_b = 1.72$ is near the minimum Mach number for given beam speed v_b . We remark that the data setting is the same as that in [47] but the EOS is different. Initially, the computational domain $[0, 12] \times [0, 30]$ is filled with a static uniform medium with an unit rest-mass density, and a light relativistic jet is injected in the y -direction through the inlet part $|x| \leq 0.5$ on the bottom boundary ($y = 0$) with a high speed v_b , a rest-mass density of 0.01, and a pressure equal to the ambient pressure. The fixed inflow beam condition is specified on the nozzle $\{y = 0, |x| \leq 0.5\}$, the reflecting boundary condition is specified at $x = 0$, whereas the outflow boundary conditions are on other boundaries. The following three different cases are considered:

- (i) $v_b = 0.99$, corresponding to the case of $\gamma \approx 7.089$ and $M_r \approx 9.971$.
- (ii) $v_b = 0.999$, corresponding to the case of $\gamma \approx 22.366$ and $M_r \approx 31.316$.
- (iii) $v_b = 0.9999$, corresponding to the case of $\gamma \approx 70.712$ and $M_r \approx 98.962$.

Here $M_r := M_b \gamma / \gamma_s$ denotes the relativistic Mach number with $\gamma_s = 1/\sqrt{1 - c_s^2}$ being the Lorentz factor associated with the local sound speed.

As v_b becomes much closer to the speed of light, the simulation of the jet becomes more challenging. Figures 4.11-4.14 display the schlieren images of the rest-mass density logarithm $\ln \rho$ and the pressure logarithm $\ln p$ within the domain $[-12, 12] \times [0, 30]$ at $t = 30$ obtained by using the first- and the fifth-order schemes on 240×600 uniform meshes for the computational domain $[0, 12] \times [0, 30]$. It is clear to observe that the high-order scheme can capture the beam interfaces much better than the first-order scheme.

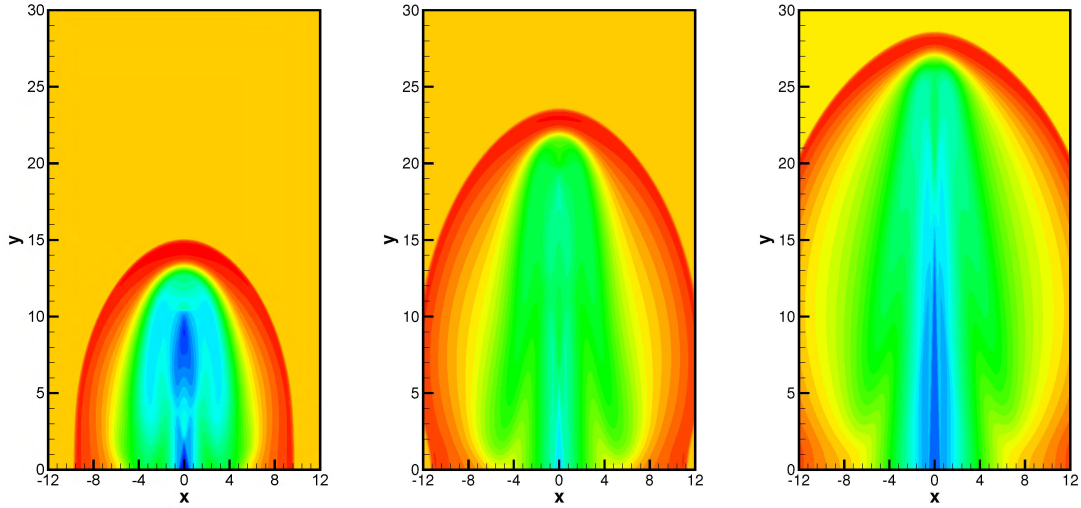


Figure 4.11: Example 4.6: Schlieren images of rest-mass density logarithm $\ln \rho$ at $t = 30$ for the hot jet model obtained by the first-order PCP scheme with 240×600 uniform cells. From left to right: configurations (i), (ii) and (iii).

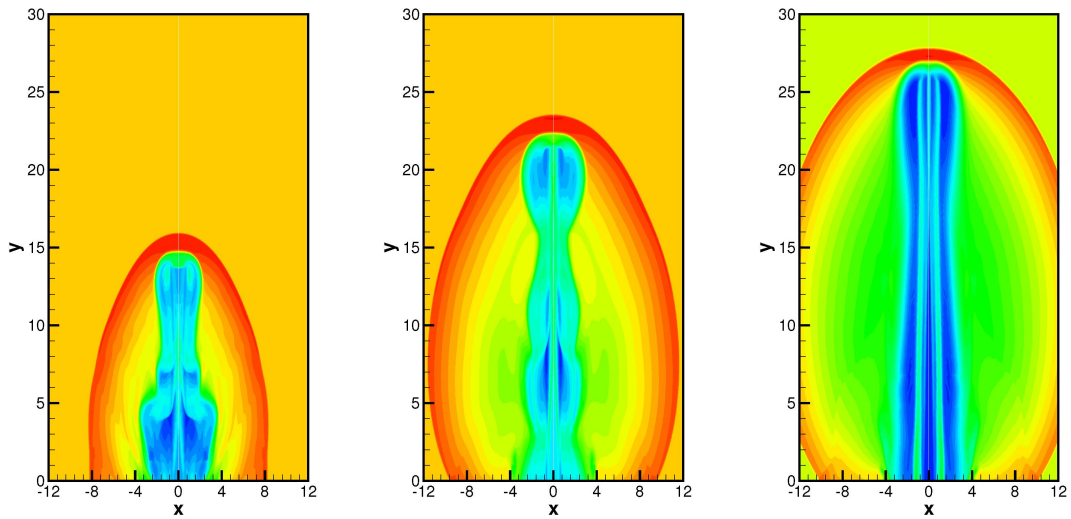


Figure 4.12: Example 4.6: Same as Figure 4.11 except for the fifth-order PCP scheme.

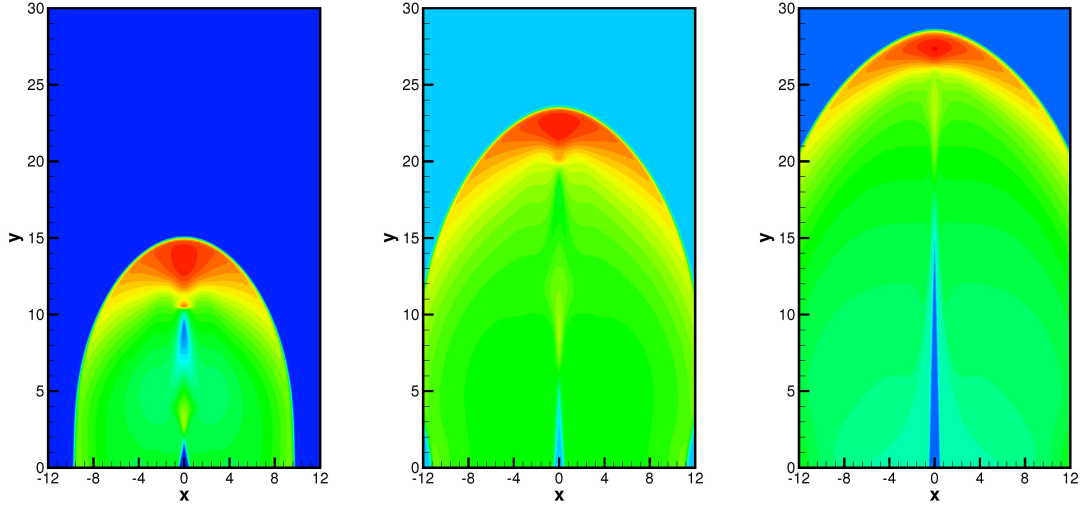


Figure 4.13: Example 4.6: Schlieren images of pressure logarithm $\ln p$ at $t = 30$ for the hot jet model obtained by the first-order PCP scheme with 240×600 uniform cells. From left to right: configurations (i), (ii) and (iii).

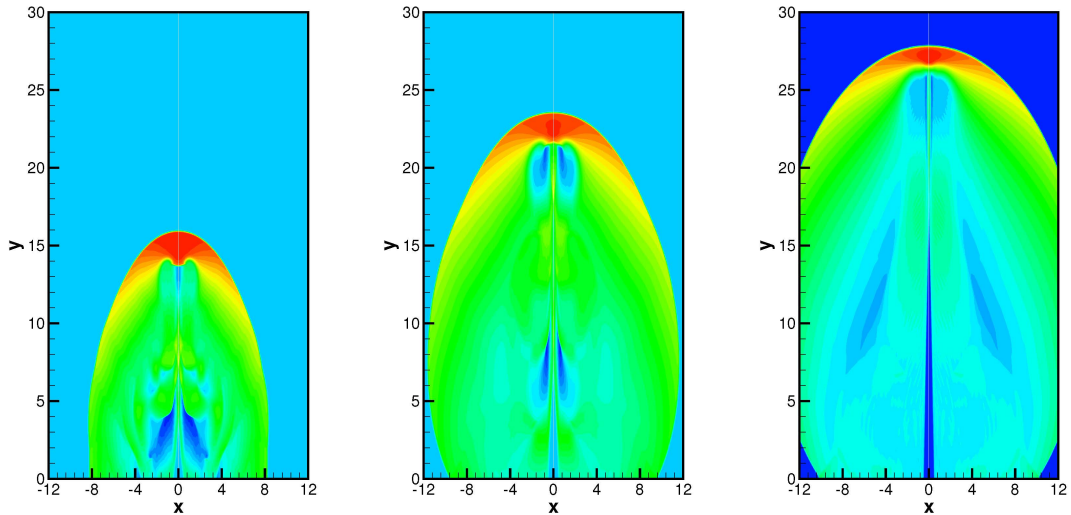


Figure 4.14: Example 4.6: Same as Figure 4.13 except for the fifth-order PCP scheme.

5 Conclusion

This paper proposed a finite volume scheme based on the multidimensional HLL Riemann solver for the 2D special relativistic hydrodynamics and then studied its PCP property (i.e., preserving the positivity of the rest-mass density and the pressure and the boundness of the fluid

velocity). We first proved that the intermediate states in the multidimensional HLL Riemann solver were PCP when the HLL wave speeds were estimated suitably, and then showed the first-order accurate finite volume scheme with the multidimensional HLL Riemann solver and forward Euler time discretization was PCP. Based on the resulting multidimensional HLL solver, we developed the higher-order accurate PCP scheme by using the high-order accurate strong stability preserving (SSP) time discretization, the WENO reconstruction procedure, and the PCP flux limiter. Finally, several 2D numerical experiments were conducted to demonstrate the accuracy and the effectiveness of the proposed PCP scheme in solving the special RHD problems involving large Lorentz factor, or low rest-mass density or low pressure or strong discontinuities, etc.

Acknowledgments

The work was partially supported by the National Key R&D Program of China (Project Number 2020YFA0712000). Moreover, D. Ling would like to acknowledge support by the National Natural Science Foundation of China (Grant No. 12101486), the China Postdoctoral Science Foundation (Grant No. 2020M683446), and the High-performance Computing Platform at Xi'an Jiaotong University; H.Z. Tang would like to acknowledge support by the National Natural Science Foundation of China (Grant No. 12171227 & 12288101).

Appendix A Proof of Lemma 1.2

This appendix provides a proof of Lemma 1.2, which is slightly different from that of Lemma 2.3 in [45]. Noting that the second and third properties in Lemma 1.2 are formally different from those in Lemma 2.3 of [45].

(i) For any positive number κ , let $(D^\kappa, \mathbf{m}^\kappa, E^\kappa)^T = \mathbf{U}^\kappa := \kappa \mathbf{U}$. Since $\mathbf{U} \in \mathcal{G}$, it is easy to verify

$$D^\kappa = \kappa D > 0, \quad E^\kappa - \sqrt{(D^\kappa)^2 + |\mathbf{m}^\kappa|^2} = \kappa(E - \sqrt{D^2 + |\mathbf{m}|^2}) > 0,$$

which leads to admissibility of $\kappa \mathbf{U}$.

(ii) The convexity of \mathcal{G} shows

$$\frac{a_1}{a_1 + a_2} \mathbf{U}_1 + \frac{a_2}{a_1 + a_2} \mathbf{U}_2 \in \mathcal{G},$$

for any $a_1, a_2 > 0$ and $\mathbf{U}_1, \mathbf{U}_2 \in \mathcal{G}$. Combining it with the conclusion in (i) yields

$$a_1 \mathbf{U}_1 + a_2 \mathbf{U}_2 \in \mathcal{G}.$$

(iii) For simplicity, denote

$$\begin{aligned} (D^\alpha, \mathbf{m}_i^\alpha, E^\alpha)^T &= \mathbf{U}^\alpha := \alpha \mathbf{U} - \mathbf{F}_i(\mathbf{U}), \\ (D^\beta, \mathbf{m}_i^\beta, E^\beta)^T &= \mathbf{U}^\beta := -\beta \mathbf{U} + \mathbf{F}_i(\mathbf{U}). \end{aligned}$$

For the state \mathbf{U}^α with $\alpha \geq \lambda_i^{(4)}(\mathbf{U})$, we can get

$$\begin{aligned} D^\alpha &= D(\alpha - u_i) \geq D(\lambda_i^{(4)}(\mathbf{U}) - u_i) > 0, \\ E^\alpha &= E(\alpha - u_i) - pu_i \geq E(\lambda_i^{(4)}(\mathbf{U}) - u_i) - pu_i \\ &= \frac{p\gamma^2}{c_s^2} \left((\Gamma - c_s^2 \gamma^{-2}) \frac{u_i(1 - c_s^2) + c_s \gamma^{-1} \sqrt{1 - u_i^2 - c_s^2(|\mathbf{u}|^2 - u_i^2)}}{1 - c_s^2 |\mathbf{u}|^2} - \Gamma u_i \right) \\ &\geq \frac{p\gamma^2}{c_s^2} \left((\Gamma - c_s^2 \gamma^{-2}) \frac{u_i(1 - c_s^2) + c_s \gamma^{-2}}{1 - c_s^2 |\mathbf{u}|^2} - \Gamma u_i \right) \\ &= \frac{p}{c_s(1 - c_s^2 |\mathbf{u}|^2)} \left(-c_s u_i (\Gamma - c_s^2 + 1) + \Gamma - c_s^2 \gamma^{-2} \right) \\ &\geq \frac{p}{c_s(1 - c_s^2 |\mathbf{u}|^2)} \left(-c_s |\mathbf{u}| (\Gamma - c_s^2 + 1) + \Gamma - c_s^2 \gamma^{-2} \right) \\ &= \frac{p}{c_s(1 + c_s |\mathbf{u}|)} \left(\Gamma - c_s^2 - c_s |\mathbf{u}| \right) > 0, \end{aligned}$$

and

$$\begin{aligned} (E^\alpha)^2 - |\mathbf{m}^\alpha|^2 - (D^\alpha)^2 &= (E^2 - |\mathbf{m}|^2 - D^2 - p^2)(\alpha - u_i)^2 + p^2(\alpha^2 - 1) \\ &= \frac{\Gamma p^2}{c_s^2} \gamma^2 \left(\frac{2}{\Gamma - 1} - \frac{\Gamma c_s^2}{(\Gamma - 1)^2} \right) (\alpha - u_i)^2 + p^2(\alpha^2 - 1) \\ &= p^2 \cdot f(\alpha), \end{aligned}$$

where $f(s)$ is a quadratic function of $s \in [\lambda_i^{(4)}(\mathbf{U}), 1)$ with the form of

$$f(s) = \frac{\Gamma \gamma^2}{c_s^2} \left(\frac{2}{\Gamma - 1} - \frac{\Gamma c_s^2}{(\Gamma - 1)^2} \right) (s - u_i)^2 + s^2 - 1.$$

It is easy to prove that $f(s)$ is monotonically increasing with $s \in [\lambda_i^{(4)}(\mathbf{U}), 1)$, so that $f(s) \geq f(\lambda_i^{(4)}(\mathbf{U}))$ for any $s \in [\lambda_i^{(4)}(\mathbf{U}), 1)$ and then $f(\alpha) \geq f(\lambda_i^{(4)}(\mathbf{U}))$. Moreover, we have

$$\begin{aligned} f(\lambda_i^{(4)}(\mathbf{U})) &= \frac{2\Gamma(\Gamma-1) - \Gamma^2 c_s^2}{(\Gamma-1)^2(1-c_s^2|\mathbf{u}|^2)^2} \left(-\frac{c_s u_i}{\gamma} + \sqrt{1-u_i^2 - c_s^2(|\mathbf{u}|^2 - u_i^2)} \right)^2 \\ &\quad + \frac{\left(u_i(1-c_s^2) + c_s \gamma^{-1} \sqrt{1-u_i^2 - c_s^2(|\mathbf{u}|^2 - u_i^2)} \right)^2}{(1-c_s^2|\mathbf{u}|^2)^2} - 1 \\ &= C_1 \left(c_s u_i \gamma^{-1} - \sqrt{1-u_i^2 - c_s^2(|\mathbf{u}|^2 - u_i^2)} \right)^2 \geq 0, \end{aligned}$$

with

$$C_1 = \frac{1}{(1-c_s^2|\mathbf{u}|^2)^2} \left(\Gamma^2 - 1 + c_s^2(1-2\Gamma) \right) > 0.$$

Therefore, $f(\alpha) > 0$ and then $(E^\alpha)^2 - |\mathbf{m}^\alpha|^2 - (D^\alpha)^2 > 0$. So far, we have proved the conclusion $\alpha\mathbf{U} - \mathbf{F}(\mathbf{U}) \in \mathcal{G}$ for $\alpha \geq \lambda_i^{(4)}(\mathbf{U})$.

For the state \mathbf{U}^β with $\beta \leq \lambda_i^{(1)}(\mathbf{U})$, one can similarly have

$$\begin{aligned} D^\beta &= D(u_i - \beta) \geq D(u_i - \lambda_i^{(1)}(\mathbf{U})) > 0, \\ E^\beta &= E(u_i - \beta) + p u_i \geq E(u_i - \lambda_i^{(1)}(\mathbf{U})) + p u_i \\ &= \frac{p\gamma^2}{c_s^2} \left(-(\Gamma - c_s^2\gamma^{-2}) \frac{u_i(1-c_s^2) - c_s\gamma^{-1}\sqrt{1-u_i^2 - c_s^2(|\mathbf{u}|^2 - u_i^2)}}{1-c_s^2|\mathbf{u}|^2} + \Gamma u_i \right) \\ &\geq \frac{p\gamma^2}{c_s^2} \left(-(\Gamma - c_s^2\gamma^{-2}) \frac{u_i(1-c_s^2) - c_s\gamma^{-2}}{1-c_s^2|\mathbf{u}|^2} + \Gamma u_i \right) \\ &= \frac{p}{c_s(1-c_s^2|\mathbf{u}|^2)} \left(c_s u_i(\Gamma - c_s^2 + 1) + \Gamma - c_s^2\gamma^{-2} \right) \\ &\geq \frac{p}{c_s(1-c_s^2|\mathbf{u}|^2)} \left(-c_s|\mathbf{u}|(\Gamma - c_s^2 + 1) + \Gamma - c_s^2\gamma^{-2} \right) \\ &= \frac{p}{c_s(1+c_s|\mathbf{u}|)} \left(\Gamma - c_s^2 - c_s|\mathbf{u}| \right) > 0, \end{aligned}$$

and

$$\begin{aligned} (E^\beta)^2 - |\mathbf{m}^\beta|^2 - (D^\beta)^2 &= (E^2 - |\mathbf{m}|^2 - D^2 - p^2)(\beta - u_i)^2 + p^2(\beta^2 - 1) \\ &= \frac{\Gamma p^2}{c_s^2} \gamma^2 \left(\frac{2}{\Gamma-1} - \frac{\Gamma c_s^2}{(\Gamma-1)^2} \right) (\beta - u_i)^2 + p^2(\beta^2 - 1) \\ &= p^2 \cdot g(\beta), \end{aligned}$$

where $g(s)$ is a quadratic function of $s \in (-1, \lambda_i^{(1)}(\mathbf{U})]$ with the form of

$$g(s) = \frac{\Gamma\gamma^2}{c_s^2} \left(\frac{2}{\Gamma-1} - \frac{\Gamma c_s^2}{(\Gamma-1)^2} \right) (s - u_i)^2 + s^2 - 1.$$

It is easy to prove that $g(s)$ is monotonically decreasing with $s \in (-1, \lambda_i^{(1)}(\mathbf{U})]$, so that $g(s) \geq g(\lambda_i^{(1)}(\mathbf{U}))$ for any $s \in (-1, \lambda_i^{(1)}(\mathbf{U})]$ and then $g(\beta) \geq g(\lambda_i^{(1)}(\mathbf{U}))$. Moreover, we can show

$$\begin{aligned} g(\lambda_i^{(1)}(\mathbf{U})) &= \frac{2\Gamma(\Gamma-1) - \Gamma^2 c_s^2}{(\Gamma-1)^2(1 - c_s^2|\mathbf{u}|^2)^2} \left(c_s u_i \gamma^{-1} + \sqrt{1 - u^2 - c_s^2(|\mathbf{u}|^2 - u_i^2)} \right)^2 \\ &\quad + \frac{\left(u_i(1 - c_s^2) - c_s \gamma^{-1} \sqrt{1 - u_i^2 - c_s^2(|\mathbf{u}|^2 - u_i^2)} \right)^2}{(1 - c_s^2|\mathbf{u}|^2)^2} - 1 \\ &= C_2 \left(c_s u_i \gamma^{-1} + \sqrt{1 - u_i^2 - c_s^2(|\mathbf{u}|^2 - u_i^2)} \right)^2 \geq 0, \end{aligned}$$

with

$$C_2 = \frac{1}{(1 - c_s^2|\mathbf{u}|^2)^2} \left(\Gamma^2 - 1 + c_s^2(1 - 2\Gamma) \right) > 0.$$

Therefore, $g(\beta) > 0$ and then $(E^\beta)^2 - |\mathbf{m}^\beta|^2 - (D^\beta)^2 > 0$, which leads to $-\beta\mathbf{U} + \mathbf{F}_i(\mathbf{U}) \in \mathcal{G}$ for $\beta \leq \lambda_i^{(1)}(\mathbf{U})$. \square

References

- [1] R. Abgrall, A genuinely multidimensional Riemann solver, *Research Report*, RR-1859, 1993 (<https://hal.inria.fr/inria-00074814>).
- [2] D.S. Balsara, Multidimensional HLLC Riemann solver: Application to Euler and magnetohydrodynamic flows, *J. Comput. Phys.*, 229 (2010) 1970-1993.
- [3] D.S. Balsara, A two-dimensional HLLC Riemann solver for conservation laws: Application to Euler and magnetohydrodynamic flow, *J. Comput. Phys.*, 231 (2012) 7476-7503.
- [4] D.S. Balsara, M. Dumbser and R. Abgrall, A multidimensional HLLC Riemann solver for unstructured meshes-With application to Euler and MHD flows, *J. Comput. Phys.*, 261 (2014) 172-208.

- [5] D.S. Balsara and M. Dumbser, Divergence-free MHD on unstructured meshes using high order finite volume schemes based on multidimensional Riemann solvers, *J. Comput. Phys.*, 299 (2015) 687-715.
- [6] P. Batten, N. Clarke, C. Lambert and D.M. Causon, On the choice of wavespeeds for the HLLC Riemann solver, *SIAM J. Sci. Comput.*, 18 (1997) 1553-1570.
- [7] B. Biswasa, H. Kumarb and D. Bhorriya, Entropy stable discontinuous Galerkin schemes for the special relativistic hydrodynamics equations, *Comput. Math. Appl.*, 112 (2022) 55-75.
- [8] G. Capdeville, A multidimensional HLL-Riemann solver for Euler equations of gas dynamics, *Comput. Fluids*, 47 (2011) 122-147.
- [9] G. Capdeville, A multidimensional HLL-Riemann solver for non-linear hyperbolic systems, *Int. J. Numer. Meth. Fluids*, 67 (2011) 1899-1931.
- [10] P. Colella, A direct Eulerian MUSCL scheme for gas dynamics, *SIAM J. Sci. Stat. Comput.*, 6 (1985) 104-117.
- [11] S. F. Davis, Simplified second-order Godunov-type methods, *SIAM J. Sci. Stat. Comput.*, 9(3)(1988) 445-473.
- [12] D. Bhorriya and H. Kumar, Entropy-stable schemes for relativistic hydrodynamics equations, *Z. Angew. Math. Phys.*, 71 (2020) 1-29.
- [13] A. Dolezal and S.S.M. Wong, Relativistic hydrodynamics and essentially non-oscillatory shock capturing schemes, *J. Comput. Phys.*, 120 (1995) 266-277.
- [14] J.M. Duan and H.Z. Tang, High-order accurate entropy stable finite difference schemes for one- and two-dimensional special relativistic hydrodynamics, *Adv. Appl. Math. Mech.*, 12 (2020) 1-29.

- [15] J.M. Duan and H.Z. Tang, High-order accurate entropy stable nodal discontinuous Galerkin schemes for the ideal special relativistic magnetohydrodynamics, *J. Comput. Phys.*, 421 (2020) 109731.
- [16] J.M. Duan and H.Z. Tang, Entropy stable adaptive moving mesh schemes for 2D and 3D special relativistic hydrodynamics, *J. Comput. Phys.*, 426 (2021) 109949.
- [17] J.M. Duan and H.Z. Tang, High-order accurate entropy stable adaptive moving mesh finite difference schemes for special relativistic (magneto)hydrodynamics, *J. Comput. Phys.*, 456 (2022) 111038.
- [18] B. Einfeldt, On Godunov-type methods for gas dynamics, *SIAM J. Numer. Anal.*, 25 (3) (1988) 294-318.
- [19] J.A. Font, Numerical hydrodynamics and magnetohydrodynamics in general relativity, *Living Rev. Relativ.*, 11 (2008) 7.
- [20] A. Harten, P.D. Lax and B.van Leer, On upstream differencing and Godunov-type schemes for hyperbolic conservation laws, *SIAM Rev.*, 25 (1983) 289-315.
- [21] P. He and H.Z. Tang, An adaptive moving mesh method for two-dimensional relativistic hydrodynamics, *Commun. Comput. Phys.*, 11 (2012) 114-146.
- [22] P. He and H.Z. Tang, An adaptive moving mesh method for two-dimensional relativistic magnetohydrodynamics, *Comput. Fluids*, 60 (2012) 1-20.
- [23] D. Ling, J.M. Duan and H.Z. Tang, Physical-constraints-preserving Lagrangian finite volume schemes for one-and two-dimensional special relativistic hydrodynamics, *J. Comput. Phys.*, 396 (2019) 507-543.
- [24] F.D. Lora-Clavijo, J.P. Cruz-Pérez, F.S. Guzmán and J.A. González, Exact solution of the 1D Riemann problem in Newtonian and relativistic hydrodynamics, *Rev. Mex. Fís. E*, 59 (2013) 28-50.

- [25] J.C. Mandal and V. Sharma, A genuinely multidimensional convective pressure flux split Riemann solver for Euler equations, *J. Comput. Phys.*, 297 (2015) 669-688.
- [26] J.M. Martí and E. Müller, The analytical solution of the Riemann problem in relativistic hydrodynamics, *J. Fluid Mech.*, 258 (1994) 317-333.
- [27] J.M. Martí and E. Müller, Numerical hydrodynamics in special relativity, *Living Rev. Relativ.*, 6 (2003) 7.
- [28] J.M. Martí and E. Müller, Grid-based methods in relativistic hydrodynamics and magnetohydrodynamics, *Living Rev. Comput. Astrophys.*, 1 (2015) 3.
- [29] M.M. May and R.H. White, Hydrodynamics calculations of general-relativistic collapse, *Phys. Rev.*, 141 (1966) 1232-1241.
- [30] M.M. May and R.H. White, Stellar dynamics and gravitational collapse, *Methods Comput. Phys.*, 7 (1967) 219-258.
- [31] V. Pant, Global entropy solutions for isentropic relativistic fluid dynamics, *Commun. Part. Diff. Eq.*, 21 (1996) 1609-1641.
- [32] T. Qin, C.-W. Shu and Y. Yang, Bound-preserving discontinuous Galerkin methods for relativistic hydrodynamics, *J. Comput. Phys.*, 315 (2016) 323-347.
- [33] F. Qu, D. Sun, J. Bai and C. Yan, A genuinely two-dimensional Riemann solver for compressible flows in curvilinear coordinates, *J. Comput. Phys.*, 386 (2019) 47-63.
- [34] D. Radice and L. Rezzolla, Discontinuous Galerkin methods for general-relativistic hydrodynamics: formulation and application to spherically symmetric spacetimes, *Phys. Rev. D*, 84 (2011) 024010.
- [35] P.L. Roe, Approximate Riemann solver, parameter vectors and difference schemes, *J. Comput. Phys.*, 43 (1981) 357-372.

- [36] K.A. Schneider, J.M. Gallardo, D.S. Balsara, B. Nkonga and C. Parés, Multidimensional approximate Riemann solvers for hyperbolic nonconservative systems. Applications to shallow water systems, *J. Comput. Phys.*, 444 (2021) 110547.
- [37] C.-W. Shu, High order weighted essentially non-oscillatory schemes for convection dominated problems, *SIAM Rev.*, 51 (2009) 82-126.
- [38] A. Tchekhovskoy, J.C. McKinney and R. Narayan, WHAM: a WENO-based general relativistic numerical scheme, I. hydrodynamics, *Mon. Not. R. Astron. Soc.*, 379 (2007) 469-497.
- [39] E.F. Toro, *Riemann Solvers and Numerical Methods for Fluid Dynamics: A Practical Introduction*, 3rd edition, Springer, 2009.
- [40] B. van Leer, Progress in multi-dimensional upwind differencing. In: Napolitano M., Sabetta F. (eds) *Thirteenth International Conference on Numerical Methods in Fluid Dynamics*, Lecture Notes in Physics, vol 414. Springer, Berlin, Heidelberg, 1993.
- [41] B. Wendroff, A two-dimensional HLLE Riemann solver and associated Godunov-type difference scheme for gas dynamics, *Comput. Math. Appl.*, 38 (1999) 175-185.
- [42] J.R. Wilson, Numerical study of fluid flow in a Kerr space, *Astrophys. J.*, 173 (1972) 431-438.
- [43] K.L. Wu, Design of provably physical-constraint-preserving methods for general relativistic hydrodynamics, *Phys. Rev. D*, 95 (2017) 103001.
- [44] K.L. Wu and H.Z. Tang, Finite volume local evolution Galerkin method for two-dimensional special relativistic hydrodynamics, *J. Comput. Phys.*, 256 (2014) 277-307.
- [45] K.L. Wu and H.Z. Tang, High-order accurate physical-constraints-preserving finite difference WENO schemes for special relativistic hydrodynamics, *J. Comput. Phys.*, 298 (2015) 539-564.

- [46] K.L. Wu and H.Z. Tang, A direct Eulerian GRP scheme for spherically symmetric general relativistic hydrodynamics, *SIAM J. Sci. Comput.*, 38 (2016) B458-B489.
- [47] K.L. Wu and H.Z. Tang, Physical-constraints-preserving central discontinuous Galerkin methods for special relativistic hydrodynamics with a general equation of state, *Astrophys. J. Suppl. Ser.*, 228 (2017) 3.
- [48] K.L. Wu and H.Z. Tang, Admissible states and physical-constraints-preserving schemes for relativistic magnetohydrodynamic equations, *Math. Models Methods Appl. Sci.*, 27 (2017) 1871-1928.
- [49] K.L. Wu and H.Z. Tang, On physical-constraints-preserving schemes for special relativistic magnetohydrodynamics with a general equation of state, *Z. Angew. Math. Phys.*, 69 (2018) 84.
- [50] K.L. Wu, Z.C. Yang and H.Z. Tang, A third-order accurate direct Eulerian GRP scheme for one-dimensional relativistic hydrodynamics, *East Asian J. Appl. Math.*, 4 (2014) 95-131.
- [51] Z.F. Xu, Parameterized maximum principle preserving flux limiters for high order schemes solving hyperbolic conservation laws: one-dimensional scalar problem, *Math. Comput.*, 83 (2014) 2213-2238.
- [52] Z.C. Yang, P. He and H.Z. Tang, A direct Eulerian GRP scheme for relativistic hydrodynamics: one-dimensional case, *J. Comput. Phys.*, 230 (2011) 7964-7987.
- [53] Z.C. Yang and H.Z. Tang, A direct Eulerian GRP scheme for relativistic hydrodynamics: two-dimensional case, *J. Comput. Phys.*, 231 (2012) 2116-2139.
- [54] Y.H. Yuan and H.Z. Tang, Two-stage fourth-order accurate time discretizations for 1D and 2D special relativistic hydrodynamics, *J. Comput. Math.*, 38 (2020) 746-774.
- [55] L.D. Zanna and N. Bucciantini, An efficient shock-capturing central-type scheme for multidimensional relativistic flows, I: hydrodynamics, *Astron. Astrophys.*, 390 (2002) 1177-1186.

- [56] X.X. Zhang and C.-W. Shu, On positivity-preserving high order discontinuous Galerkin schemes for compressible Euler equations on rectangular meshes, *J. Comput. Phys.*, 229 (2010) 8918-8934.
- [57] J. Zhao and H.Z. Tang, Runge-Kutta discontinuous Galerkin methods with WENO limiter for the special relativistic hydrodynamics, *J. Comput. Phys.*, 242 (2013) 138-168.
- [58] J. Zhao and H.Z. Tang, Runge-Kutta discontinuous Galerkin methods for the special relativistic magnetohydrodynamics, *J. Comput. Phys.*, 343 (2017) 33-72.
- [59] J. Zhao and H.Z. Tang, Runge-Kutta central discontinuous Galerkin methods for the special relativistic hydrodynamics, *Commun. Comput. Phys.*, 22 (2017) 643-682.